Atom-interferometric techniques for measuring uniform magnetic field gradients and gravitational acceleration

B. Barrett, I. Chan, and A. Kumarakrishnan
Department of Physics & Astronomy, York University, Toronto, Ontario M3J 1P3, Canada
(Received 22 April 2011; revised manuscript received 8 October 2011; published 19 December 2011)

We discuss techniques for probing the effects of a constant force acting on cold atoms using two configurations of a grating echo-type atom interferometer. Laser-cooled samples of ^{85}Rb with temperatures as low as 2.4 μK have been achieved in a new experimental apparatus with a well-controlled magnetic environment. We demonstrate interferometer signal lifetimes approaching the transit time limit in this system ($\sim$270 ms), which is comparable to the time scale achieved by Raman interferometers. Using these long time scales, we experimentally investigate the influence of a homogeneous magnetic field gradient using two- and three-pulse interferometers, which enable us to sense changes in externally applied magnetic field gradients as small as $\sim 4 \times 10^{-5}$ G/cm. We also provide an improved theoretical description of signals generated by both interferometer configurations that accurately models experimental results. With this theory, absolute measurements of B gradients at the level of 3×10^{-4} G/cm are achieved. Finally, we contrast the suitability of the two- and three-pulse interferometers for precision measurements of the gravitational acceleration, g.

DOI: 10.1103/PhysRevA.84.063623 PACS number(s): 37.25.+k, 03.75.−b, 07.55.Ge, 04.80.−y

I. INTRODUCTION

Atom interferometers (AIs) have been employed to investigate a host of inertial effects over the past few decades. Such effects include the acceleration due to gravity [1–5], gravity gradients [6–8], and rotations [9–11]. Raman interferometric measurements of gravity [1–3] use cold atoms and transit time-limited experiments in an atomic fountain to reach a precision of $\sim$3 parts per 10^9 (ppb) with 1 min of interrogation time. This technique requires two phase-locked lasers to drive Raman transitions between two hyperfine ground states. It also requires state selection into the $m_F = 0$ magnetic sublevel to avoid sensitivity to B fields and B gradients, as well as velocity selection to guarantee that all interfering atoms have the same initial subrecoil velocity.

In contrast to the Raman interferometer, the grating echo-type AI [12,13] uses a single off-resonant excitation frequency that drives a cycling transition with the same initial and final state. This AI requires no internal state or velocity selection, and has reduced sensitivity to both the ac Stark effect (which scales inversely with the excitation field detuning) and the Zeeman effect. Additionally, as we will show on the basis of a theoretical model, the intensity of the AI signal is insensitive to uniform B gradients provided the atoms are pumped into a single magnetic sublevel—which need not be $m_F = 0$.

In this work, we use two configurations of the grating echo AI to demonstrate experiments with time scales comparable to those of Raman AIs. An improved theoretical description of the echo AI has enabled accurate modeling of experimental data from which sensitive measurements of an externally applied B gradient can be extracted. This model is sufficiently general to describe many time-domain configurations of grating echo AIs, while accounting for a constant force on the atoms, as well as the sublevel structure of the atomic ground state. Recent work [14] has shown that measurements of the phase of the electric field are less sensitive to mirror vibrations with a particular configuration of this AI. Here, we investigate the influence of B gradients on the same AI configuration, which validates our predictions of gravitational effects, and indicates that this AI is particularly well suited for precise measurements of the gravitational acceleration g.

We begin with a review of the two AI configurations used in this work, which are illustrated in Fig. 1. The two-pulse echo AI [12,13,15,16] utilizes short (Raman-Nath) standing wave (sw) pulses to diffract a sample of laser-cooled atoms at $t = T_1$ into a superposition of momentum states: $|n\hbar\boldsymbol{q}\rangle$. Here, n is an integer and $\boldsymbol{q} = \boldsymbol{k}_1 - \boldsymbol{k}_2 \approx 2\boldsymbol{k}$ is the difference between the traveling wave vectors comprising the sw. At $t = T_2$, a second sw pulse further diffracts the atomic wave packets—creating sets of center-of-mass trajectories that overlap and produce interference in the form of a density modulation in the vicinity of $t^{(2)}_{\text{echo}} = T_1 + (\bar{N} + 1)T_{21}$, where $T_{21} \equiv T_2 - T_1$ and $\bar{N} = 1,2,\ldots$ is the order of the echo, as shown in Fig. 1(a). The induced density modulation is coherent for $\tau_{\text{coh}} = 2/q\sigma_v \sim 3$ μs about these "echo" times, beyond which the modulation dephases due to the distribution of velocities in the sample. Here, $\sigma_v = (2k_B\mathcal{T}/M)^{1/2}$ characterizes the width of the velocity distribution along $\hat{z}$. A traveling wave pulse is applied along the $\hat{z}$ direction in the vicinity of $t^{(2)}_{\text{echo}}$ to "read out" the amplitude of the grating by coherently Bragg scattering light along the $-\hat{z}$ direction. The duration of this signal is limited by the coherence time τ_{coh}. Due to the nature of Bragg diffraction, this back-scattered light is proportional to the Fourier component of the density distribution with spatial frequency q. This harmonic is only produced by the interference of momentum states that differ by $\hbar q$ ($\Delta n = \pm 1$). As a result, the two-pulse AI exhibits a temporal modulation at the two-photon atomic recoil frequency, $\omega_q = \hbar q^2/2M$, and is therefore sensitive to recoil effects.

The three-pulse "stimulated" grating echo AI (henceforth referred to as the three-pulse AI) was first demonstrated in Ref. [13] using a single hyperfine ground state, and was termed a "stimulated" echo due to similarities in pulse geometry with the stimulated photon echo scheme [17–20]]. Recent work involving this interferometer [14] has shown certain advantages over the two-pulse scheme for phase measurements of the atomic grating. The three-pulse AI involves applying

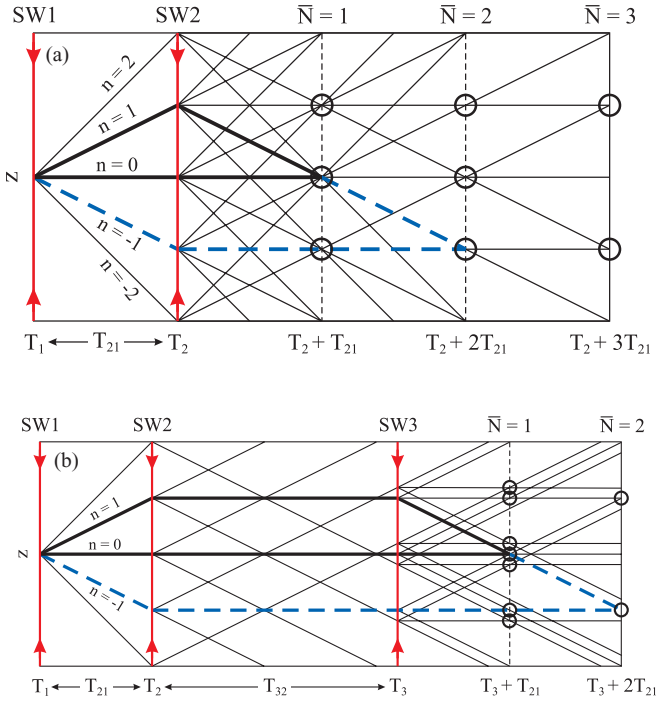

FIG. 1. (Color online) Recoil diagrams for the two-pulse (a) and three-pulse (b) AIs in the absence of any external forces. Standing wave excitations are labeled by SW1–SW3. At $t = T_1$ the atom is diffracted into a superposition of momentum states differing by integer (n) multiples of $\hbar q$. A second sw pulse is applied at $t = T_2$ which further diffracts the atoms. In the two-pulse case, interference between states differing by $\hbar q$ ($\Delta n = \pm 1$) occurs at times $t^{(2)}_{\text{echo}} = T_1 + (\bar{N} + 1)T_{21}$. For the three-pulse scheme, a third sw pulse is applied at $t = T_3$ which produces interference at times $t^{(3)}_{\text{echo}} = T_1 + (\bar{N} + 1)T_{21} + T_{32}$. Examples of interfering trajectories for $\bar{N} = 1$ and 2 are labeled by solid black and dashed blue lines, respectively. Circles indicate locations where interference fringes occur with spatial frequency q.

two sw pulses at $t = T_1$ and $t = T_2$, followed by a third pulse applied at $t = T_3 = T_2 + T_{32}$. This pulse geometry produces an echo in the vicinity of $t^{(3)}_{\text{echo}} = T_1 + (\bar{N} + 1)T_{21} + T_{32}$, as shown in Fig. 1(b). However, unlike the two-pulse AI where all pairs of trajectories produced by the second pulse interfere at the echo times, for the three-pulse AI only momentum states of the same order ($\Delta n = 0$) after the second pulse produce interference at the echo times for arbitrary T_{21} and T_{32}. For this reason, the signal produced by this interferometer as a function of T_{32} (with T_{21} fixed) is insensitive to atomic recoil (i.e., no temporal modulation) and is therefore ideal for probing other effects—such as those due to a constant force on the atoms.

Reference [21] extensively reviews the grating echo AI and discusses applications relating to atomic recoil [15,16,22–25], gravity, and magnetic gradients [26].

Previous experiments based on this AI [12,13,15,16,22–24,27] were typically limited to $T_{21} < 10$ ms by decoherence effects due to spatially and temporally varying B fields. Additionally, the sample temperature (typically $\sim$50 μK) and excitation beam configuration (fixed frequency sw with $\sim$0.5 cm diameter) limited the transit time in these experiments. In this work, we have improved the level of B-field and B-gradient suppression by using a nonmagnetic vacuum chamber, which has enabled the extension of AI signal lifetimes. The magnetically controlled environment allows a sample of ^{85}Rb atoms to be cooled to temperatures as low as 2.4 μK. By expanding the excitation beam diameter to $\sim$2 cm, and chirping the sw pulses to cancel Doppler shifts, echo AI signal lifetimes of $\sim$220 ms and transit times of $\sim$270 ms have been achieved. These time scales are comparable to those of fountain experiments involving Raman AIs [1,2,28]. To the best of our knowledge, long-lived grating echo AI signals have so far only been observed by using magnetic guides to limit transverse cloud expansion [14].

The experimental apparatus presented here has made it possible to exploit the aforementioned advantages of the grating echo AI for a variety of precision measurements, such as the atomic recoil frequency [25] and the gravitational acceleration [21], that are currently underway. Additionally, we recently utilized this apparatus to perform a coherent transient experiment with cold Rb atoms to achieve a precise determination of the atomic g-factor ratio [29].

In this article, we utilize long-lived signals to investigate the effects of B gradients using both the two-pulse and three-pulse grating echo AIs [13,14]. The influence of B gradients on AI experiments is of interest for precise measurements of g, and has been considered in the past. Reference [30] calculates how both gravity and B gradients affect the visibility of interference patterns in atomic diffraction experiments. A Raman AI is used in Ref. [30] to map spatial variations in the B gradient along the trajectory of an atomic fountain. In previous work [26], we demonstrated the effect of both gravity and B gradients on the two-pulse grating echo AI. A theoretical description of these effects based on a spin-1/2 system was able to explain the basic signal dependence on the pulse separation, T_{21}, but was insufficient to model experimental data.

This work relies on an improved theoretical description of a generalized grating echo AI that includes an arbitrary number of sw excitation pulses, the effects of a constant force on the atoms, spontaneous emission, and the sublevel structure of the atomic ground state (the $5S_{1/2}$ $F = 3$ state of ^{85}Rb is used in experiments). Coupled with these theoretical predictions, we achieve sensitivity to *changes* in B gradients at the level of $\sim 4 \times 10^{-5}$ G/cm. This quantity is comparable to the $\sim 3 \times 10^{-5}$ G/cm resolution recently achieved using a Raman interferometric technique [31]. In addition, absolute measurements of B gradients as small as 3×10^{-4} G/cm, and sensitivity to the curvature of B fields are demonstrated. These studies help place limits on the sensitivity of a broad class of time-domain AIs to B gradients.

We also consider implications for achieving precise measurements of g using the two- and three-pulse grating echo AIs. In particular, analysis of the three-pulse AI suggests there are significant advantages for measuring g over the two-pulse AI. Although the experimental apparatus used in this work is not designed to detect gravitational effects, predictions of the grating phase modulation due to gravity for both AIs have been validated by measuring the effects of externally applied B gradients. Measurements of g using these AIs will be presented elsewhere.

This article is organized as follows. In Sec. II we present theoretical predictions for the two- and three-pulse AI signals

in the presence of a uniform B gradient. In Sec. III, we describe details related to the experimental apparatus. We present the results of experiments related to long signal lifetimes in Sec. IV, and discuss measurements of B gradients using both the two-pulse and three-pulse techniques. Section V discusses the feasibility of a precise measurement of g using the formalism developed to describe B gradients. We conclude in Sec. VI. The Appendix presents a calculation of the signal generated by a generalized grating echo AI—encompassing the two- and three-pulse AIs—in the presence of a constant force.

II. THEORY

In this section, we present the key results of calculations for both the two- and three-pulse AI signals in the presence of a homogeneous B gradient. Details of the calculations—which are sufficiently general to account for any constant force on the atoms, and an arbitrary number of excitation pulses—are presented in the Appendix.

In general, the sensitivity of these interferometers can be characterized by the space-time area they enclose. Since only those states differing by $\hbar q$ at the echo time contribute to the signal, the area of both AIs is primarily controlled by T_{21}. In the absence of any external forces, the areas of the two- and three-pulse AIs can be calculated by inspecting their recoil diagrams [Figs. 1(a) and 1(b), respectively]:

$$A^{(2)} = \frac{\hbar q}{2M}\bar{N}(\bar{N}+1)\left(T_{21}^{(2)}\right)^2, \tag{1a}$$

$$A^{(3)} = \frac{\hbar q}{2M}\left[\bar{N}(\bar{N}+1)\left(T_{21}^{(3)}\right)^2 + 2\bar{N}T_{32}T_{21}^{(3)}\right], \tag{1b}$$

where M is the mass of the atom. Henceforth, quantities containing superscripts (2) or (3) indicate the interferometer for which that quantity applies. At first glance, it might appear that the three-pulse AI encloses a larger area than the two-pulse AI due to the extra term in Eq. (1b). However, one must compare the enclosed areas at the same echo times, which are given by $t_{\text{echo}}^{(2)} = T_1 + (\bar{N}+1)T_{21}^{(2)}$ and $t_{\text{echo}}^{(3)} = T_1 + (\bar{N}+1)T_{21}^{(3)} + T_{32}$ for the two- and three-pulse schemes, respectively. By setting $t_{\text{echo}}^{(2)} = t_{\text{echo}}^{(3)}$, it can be shown that $A^{(2)} - A^{(3)} = \hbar q \bar{N} T_{32}^2/2M(\bar{N}+1)$. This suggests that the two-pulse AI is always more sensitive to external forces than the three-pulse AI. Nevertheless, the three-pulse AI offers a unique feature: The spatial separation between interfering wave packets remains constant between the application of the second and third sw pulses. This is advantageous because larger spatial separation leads to increased decoherence, and therefore reduced time scale in the experiment [14]. Since the separation can be precisely controlled by the pulse separation T_{21}, one can increase the signal lifetime by using smaller T_{21}.

Additionally, since the signal generated by the two-pulse AI is modulated at the recoil frequency ω_q, there are periodic regions where the signal-to-noise ratio is less than one and not well suited for accurate phase measurements. However, the three-pulse technique is insensitive to atomic recoil if T_{21} is fixed. Therefore, the scattered field amplitude has no additional modulation at ω_q as T_{32} is varied—allowing regions of low signal-to-noise ratio to be avoided.

Both the gravitational force and a constant B gradient produce a constant force on the atoms, $\boldsymbol{\mathcal{F}} = \mathcal{F}\hat{z}$, which induces a phase shift in the atomic interference pattern. The basic physical mechanism that causes this phase shift is a difference in potential energy between the two arms of the AI. One can compute the relative phase between the two arms $\Delta\phi = (\mathcal{S}_{\text{B}} - \mathcal{S}_{\text{A}})/\hbar$ using the classical action [3]:

$$\mathcal{S}(t) = \int_0^t \mathcal{L}[z(t'),\dot{z}(t')]dt', \tag{2}$$

where $\mathcal{L} = M\dot{z}^2/2 + \mathcal{F}z$ is the Lagrangian in this case. If $\mathcal{S}_{\text{B}}$ and $\mathcal{S}_{\text{A}}$ represent, respectively, the action along the upper and lower arms of the two-pulse AI, it can be shown that the phase shift between these arms is

$$\Delta\phi^{(2)} = \bar{N}(\bar{N}+1)\left[\omega_q T_{21} + \frac{q\mathcal{F}}{M}T_{21}^2\right] + \bar{N}^2 q v_0 T_{21}, \tag{3}$$

where v_0 is the initial velocity of the atom along the $\hat{z}$ direction. The term proportional to v_0 is due to the relative Doppler shift between the two arms of the AI. Since the atomic sample has a finite velocity distribution (characterized by a $1/e$ radius, σ_v, and temperature $\mathcal{T}$), this term is responsible for the coherence time of the echo: $\tau_{\text{coh}} = 2/q\sigma_v$. As expected, the contribution to the phase shift from the potential energy (the term proportional to $\mathcal{F}$) is independent of the initial velocity of the cloud.

A similar calculation for the relative phase shift between the arms of the three-pulse AI yields

$$\Delta\phi^{(3)} = \bar{N}(\bar{N}+1)\left[\omega_q T_{21} + \frac{q\mathcal{F}}{M}T_{21}^2\right] + \bar{N}\frac{q\mathcal{F}}{M}T_{32}T_{21} + \bar{N}q v_0(T_{32} + \bar{N}T_{21}). \tag{4}$$

This expression is similar to Eq. (3), with additional terms proportional to the pulse spacing T_{32}. One can vary either T_{21} or T_{32} to detect phase modulation produced by an external force $\mathcal{F}$. However, since there are no terms containing the phase $\omega_q T_{32}$, one can effectively turn off the sensitivity to atomic recoil by fixing T_{21}. This makes the three-pulse AI ideal for investigating the effects due to $\mathcal{F}$, especially when $q\mathcal{F}T_{21}/M \gg \omega_q$ since no additional modulation at ω_q is present. This is particularly advantageous for measurements of gravity, as discussed in Sec. V.

Since the two-pulse AI is intrinsically more sensitive than the three-pulse AI, it is better suited to measurements of $\mathcal{F}$ when $q\mathcal{F}T_{21}/M < \omega_q$. In this work, we demonstrate this feature by measuring externally applied B gradients. The sensitivity of the three-pulse AI to $\mathcal{F}$ can be enhanced by utilizing the additional phase proportional $T_{32}T_{21}$ in Eq. (4). Experimentally, this can be accomplished by varying *both* pulse separations, T_{21} and T_{32}, with T_{21} varied in integer multiples of the recoil period: $\tau_q = \pi/\omega_q$.

We now give the main results of theoretical calculations pertaining to the response of the grating echo AI in the presence of a constant force. We have assumed a potential energy with the form,

$$\hat{U}(z) = -\hat{\mathcal{M}}\,z, \tag{5}$$

where $\hat{\mathcal{M}} = -\partial\hat{U}/\partial z$ is a matrix operator with units of force that commutes with both the position (z) and momentum (p) operators. In the case of a constant B gradient, the potential is

$$\hat{U}(z) = -\boldsymbol{\mu}\cdot\boldsymbol{B}(z) = -\frac{g_F\mu_B\beta}{\hbar}\hat{F}_z z, \tag{6}$$

where g_F is the Landé g factor, μ_B is the Bohr magneton, $\boldsymbol{B}(z) = \beta z$ is the magnetic field vector with gradient β along the z direction (also assumed to be the quantization axis), and $\hat{F}_z$ is the projection operator for total angular momentum $\boldsymbol{F}$. In this case, $\hat{\mathcal{M}} = \mathcal{F}\hat{F}_z/\hbar$ and the force is $\mathcal{F} = g_F\mu_B\beta$, where $\hat{F}_z$ operates on the basis states $|F\,m_F\rangle$ and has eigenvalues $\hbar m_F$.

In both interferometer schemes, the phase of the grating is imprinted on the electric field back-scattered from a traveling-wave read-out pulse applied in the vicinity of an echo time. For the two-pulse AI, measuring the phase of the scattered field is equivalent to measuring the relative position of the grating, since both the position and the phase scale as T_{21}^2. Similarly, in the three-pulse case, the phase measured as a function of T_{32} is proportional to the velocity of the grating—which scales as T_{21}.

We first examine the effects of B gradients on the two-pulse AI, followed by a comparison with the three-pulse AI.

A. Two-pulse interferometer

In general, the electric field scattered by the atoms at the time of an echo is proportional to the amplitude of the Fourier harmonic of the atomic density grating with spatial frequency q. For the case of an external B gradient, β, the scattered field has distinct contributions from each magnetic sublevel:

$$E_\beta^{(2)}(t;\boldsymbol{T}) = \sum_{m_F} E_{m_F}^{(2)}(t;\boldsymbol{T})e^{im_F\phi_\beta^{(2)}(t;\boldsymbol{T})}, \tag{7}$$

where $E_{m_F}^{(2)}$ is the field scattered by the state $|F\,m_F\rangle$ [given by Eq. (A21)] and $m_F\phi_\beta^{(2)}$ is the phase shift of the density grating produced by the same state in the presence of the B gradient. For the $\bar{N}^{\text{th}}$ order echo at $t_{\text{echo}}^{(2)} = T_1 + (\bar{N}+1)T_{21}$, with the set of onset times $\boldsymbol{T} = \{T_1, T_1 + T_{21}\}$ and $\Delta t = t - t_{\text{echo}}^{(2)}$, the phase shift of the grating $\phi_\beta^{(2)}(t;\boldsymbol{T})$ is given by

$$\phi_\beta^{(2)}(\Delta t; T_{21}) = \frac{qg_F\mu_B\beta}{2M}\left\{\bar{N}(\bar{N}+1)T_{21}^2 + 2[T_1 + (\bar{N}+1)T_{21}]\Delta t + \Delta t^2\right\}. \tag{8}$$

The general form of this equation for a constant force $\mathcal{F}$ is given by Eq. (A23) in the Appendix. In the discussions that follow, we take $\Delta t = 0$ which corresponds to the echo time. Since the echo lasts for $\tau_{\text{coh}} \sim 3\ \mu$s about $\Delta t = 0$, the signal is obtained by integrating the back-scattered field over this time.

Equations (7) and (8) indicate that the field amplitude scattered from state $|F\,m_F\rangle$ exhibits phase modulation as a function of T_{21} at a frequency $m_F\omega_\beta^{(2)}(T_{21})$ due to the presence of the gradient, where

$$\omega_\beta^{(2)}(T_{21}) = \left|\frac{\partial\phi_\beta^{(2)}}{\partial T_{21}}\right| = \frac{qg_F\mu_B\beta}{M}[\bar{N}(\bar{N}+1)T_{21} + (\bar{N}+1)\Delta t]. \tag{9}$$

This modulation frequency has a linear dependence on β and the pulse separation T_{21} (i.e., the frequency is chirped with T_{21}). The phase modulation of the grating produced by state $|F\ m_F\rangle$ also scales linearly with the magnetic quantum number m_F, as shown in Eq. (7). For an arbitrary set of magnetic sublevel populations, the total scattered field [Eq. (7)] contains all harmonics $m_F\omega_\beta^{(2)}(T_{21})$, where $m_F = -F,\ldots,F$. If more than one sublevel is populated, interference between the fields scattered off of each state produces modulation in the total scattered field. This effect can then be detected in the field amplitude $E_\beta^{(2)}$, or the field intensity $|E_\beta^{(2)}|^2$, by varying β or the pulse separation T_{21}. The amplitude of each harmonic comprising this modulation is determined by the sublevel populations, as well as the transition probabilities between ground and excited state sublevels.

If the system is optically pumped into a single sublevel, such as the extreme state $|F\ F\rangle$, then the phase modulation of the grating only affects the phase of the electric field—which cannot be observed using intensity detection. Instead, one can use heterodyne detection to measure the electric field amplitude and obtain the relative phase of the scattered light [12,22,26]. Furthermore, if the system is optically pumped into the $|F\ 0\rangle$ state, there is no phase modulation due to B gradients since this state is insensitive to magnetic fields.

Figures 2(a) and 2(b) show the expected two-pulse AI signal as a function of T_{21} in steps of the recoil period, $\tau_q = \pi/\omega_q$ ($\sim$32 μs for ^{85}Rb). Since $\omega_\beta^{(2)} < \omega_q$, incrementing T_{21} in this fashion eliminates additional modulation due to atomic recoil. Figure 2(a) shows the signal for equally distributed sublevel populations, while Fig. 2(b) is for an optically pumped system in the two extreme states: $|3\ {-3}\rangle$ and $|3\ 3\rangle$. Both of these figures show amplitude modulation, but in the optically pumped case there is only one frequency component present and the modulation occurs with maximum contrast—increasing the sensitivity to gradients.

Eliminating the amplitude modulation in the signal due to B gradients [shown by the dashed lines in Fig. 2(a)] is a key requirement for precision measurements of ω_q. We will show in Sec. IV that these conditions can be realized with sufficient suppression of ambient B gradients in a glass cell. It is also possible to eliminate sensitivity to B gradients using intensity detection if the atoms are pumped into a single magnetic sublevel.

B. Three-pulse interferometer

The effects due to B gradients manifest themselves differently in the three-pulse interferometer. We derive the expression for the signal in the appendix [see Eqs. (A25) and (A29)] and find that the amplitude of the scattered field does not depend on the time between the second and third sw pulses T_{32}, but only on T_{21}—similar to the two-pulse AI. However, the phase of the grating in the three-pulse case depends on both T_{21} and T_{32}:

$$\phi_\beta^{(3)}(\Delta t;\boldsymbol{T}) = \frac{qg_F\mu_B\beta}{2M}\left\{\bar{N}(\bar{N}+1)T_{21}^2 + 2\bar{N}T_{32}T_{21} + 2\left[T_1 + T_{32} + (\bar{N}+1)T_{21}\right]\Delta t + \Delta t^2\right\}. \tag{10}$$

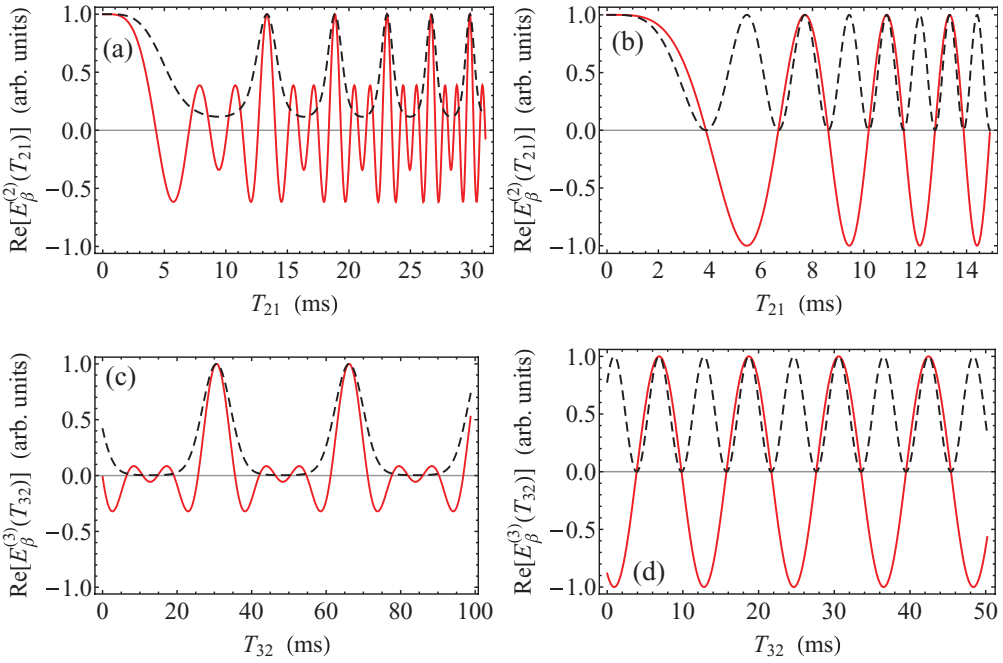

FIG. 2. (Color online) The predicted B-gradient signal for the two-pulse AI (a) and (b) [based on Eq. (7)], where T_{21} is varied in steps of $\tau_q \sim 32\ \mu$s, and the three-pulse AI (c) and (d), where T_{32} is varied. In all plots the solid red line is the real part of the scattered field, the black dashed line shows the field intensity (which is measured in the experiment), the B gradient is fixed at $\beta = 10$ mG/cm, and the first-order echo ($\bar{N} = 1$) is used. In parts (a) and (c) the excitation beams are circularly polarized ($|q_L| = 1$) and the magnetic sublevel populations are equally distributed among the $F = 3$ ground state of ^{85}Rb. In this case, the field undergoes amplitude modulation with multiple frequency components, and the field intensity exhibits modulation with a contrast <100%. For the two-pulse AI (a), the field intensity exhibits modulation at a chirped frequency, whereas for the three-pulse AI (c) the modulation is not chirped. Parts (b) and (d) show the field generated by a sample that is optically pumped equally into the $|3\ {-3}\rangle$ and $|3\ 3\rangle$ states with linearly polarized excitation beams ($q_L = 0$). Here, both the field and the field intensity exhibit modulation with only one frequency component, and the contrast of the oscillations is 100%. For both (c) and (d), T_{21} was fixed at a typical experimental value of 5 ms.

In this case, the set of pulse onset times is given by $\boldsymbol{T} = \{T_1, T_1 + T_{21}, T_1 + T_{21} + T_{32}\}$ and $\Delta t = t - t^{(3)}_{\mathrm{echo}}$. This phase is identical to Eq. (8) for the two-pulse interferometer with the addition of the two terms proportional to T_{32}. Equation (10) suggests that the force can be determined by measuring the phase modulation of the grating as a function of either T_{21} or T_{32}, or by varying both pulse separations simultaneously. Varying T_{32} produces a phase modulation of the atomic grating at a frequency that is proportional to T_{21}:

$$\omega_\beta^{(3)}(T_{21}) = \left|\frac{\partial\phi_\beta^{(3)}}{\partial T_{32}}\right| = \frac{q g_F \mu_B \beta}{M}(\bar{N} T_{21} + \Delta t). \qquad (11)$$

Figures 2(c) and 2(d) show the expected three-pulse signal as a function of T_{32}, with T_{21} fixed at a typical experimental value of 5 ms, in the presence of a B gradient $\beta = 10$ mG/cm. When the sublevel populations are equally distributed [Fig. 2(a)] the phase of the total scattered field contains multiple frequency components—one for each sublevel: $m_F \omega_\beta^{(3)}$. The interference between these components produces a modulation in the total scattered field amplitude. This is similar to the two-pulse case shown in Fig. 2(a), except that the modulation occurs at a single frequency that is fixed by β, T_{21}, and $\bar{N}$. For a sample that is optically pumped equally into the two extreme states, $|3\ {-3}\rangle$ and $|3\ 3\rangle$, as shown in Fig. 2(d), there is only one frequency component present in the scattered field, and the amplitude modulation occurs with greater contrast.

III. EXPERIMENTAL SETUP

We now review the experimental setup that has made possible long-lived grating echo AI signals. This setup is substantially different from previous echo experiments [15,23,24,26] after implementing many improvements. These include suppression of stray magnetic gradients using a nonmagnetic chamber, increasing the trapped atom number with large diameter beams, extending the transit time by cooling the sample to $\sim$10 μK and implementing large diameter excitation beams, and by chirping the excitation frequencies to eliminate Doppler shifts associated with the falling cloud.

The experiment utilizes a sample of laser-cooled ^{85}Rb atoms in a magneto-optical trap (MOT) containing approximately 10^9 atoms in a Gaussian spatial distribution with a horizontal e^{-1} radius of $\sim$1.7 mm. The MOT is contained in a borosilicate glass cell maintained at a pressure of $\sim 10^{-9}$ Torr. In addition to the anti-Helmholtz coils used for trapping, three pairs of square quadrupole coils are centered on the MOT, as shown in Fig. 3. Each square frame contains two overlapping coils, one connected in the Helmholtz configuration with a coil in the opposite frame, and the other in the anti-Helmholtz configuration. These sets of coils are used to cancel ambient

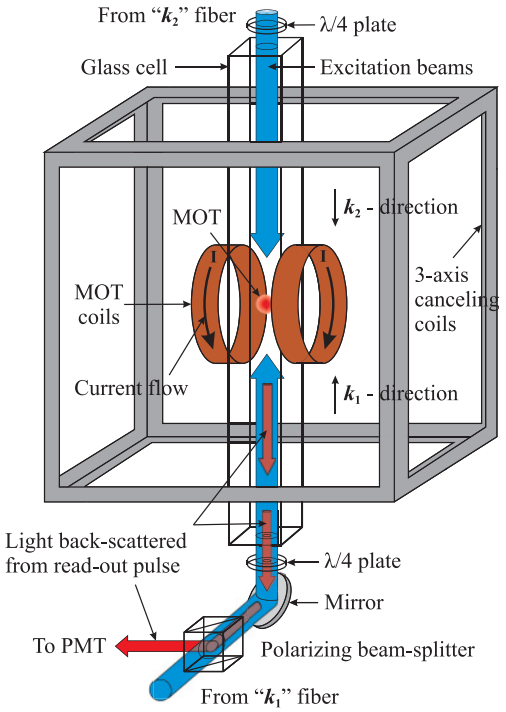

FIG. 3. (Color online) Diagram of the experiment. The excitation beams are both σ^+ polarized by the $\lambda/4$ plates. The glass cell has approximate dimensions $7.6 \times 7.6 \times 84$ cm. Each pair of square quadrupole coils has a side length of ∼66 cm and contain overlapped coils wired in both Helmholtz and anti-Helmholtz configurations for canceling B fields and B gradients, respectively.

magnetic fields and field gradients over the volume of the MOT at the level of ∼1 mG and ∼0.1 mG/cm, respectively. The initial set points for the currents in the canceling coils that produced ∼1 mG of B-field suppression were determined using an atomic magnetometer experiment [29] that allowed the field at the location of the MOT to be measured.

Light derived from a Ti:sapphire laser (linewidth ∼1 MHz) with frequency ν_L operating 130 MHz above the $5S_{1/2}$ $F = 3 \rightarrow F' = 4$ resonance frequency (ν_0) is downshifted using an acousto-optic modulator (AOM) operating in dual-pass mode, such that $\nu_L = \nu_0$. This light is locked to ν_0 using saturated absorption spectroscopy. A separate "trapping" AOM shifts this light by −148 MHz such that the detuning is $\Delta = -18$ MHz ($\nu_L = \nu_0 - 18$ MHz). Approximately 370 mW of this light is transmitted through an antireflection-coated, single-mode optical fiber (operating at 60% efficiency) and expanded to a diameter of ∼5.4 cm for trapping atoms from background vapor.

An external cavity diode laser is used to derive repump light for the trapping setup. It is locked to the $5S_{1/2}$ $F = 2 \rightarrow F' =$ (2,3) crossover transition and up-shifted by ∼32 MHz using an AOM. Approximately 25 mW of repump light is obtained after coupling through the same optical fiber as the trapping light. At $t = 0$, the MOT coils are pulsed off in ∼100 μs, while the trapping and repump beams are left on for 6 ms of molasses cooling. For ∼3 ms of this time, the detuning of the trapping light is linearly chirped from $\Delta = -18$ MHz to −50 MHz to further cool the atoms, and the power is simultaneously ramped

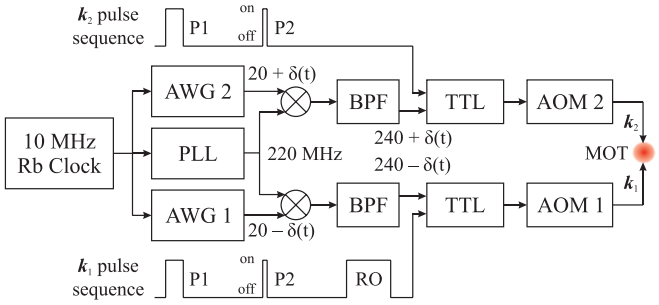

FIG. 4. (Color online) Schematic of the rf chain used for chirped AI pulses. A phase-locked loop (PLL) generates a 220-MHz rf signal which is split and mixed with the output of two separate arbitrary waveform generators (AWGs). The AWGs are triggered at the start of the experiment to output a frequency sweep from 20 MHz to 20 MHz $\pm\, \delta(t)$ after a time t, where $\delta(t) = gt/\lambda$, g∼9.8 m/s^2 and λ∼780 nm. The sum frequency from the mixers is isolated using a band-pass filter (BPF) with a center frequency of 240 MHz and a 5-dB pass band of 4 MHz. The outputs of the BPFs are pulsed using a set of transistor-transistor logic (TTL) switches, which are then sent to the k_1 and k_2 AOMs. The two-pulse AI sequence for both k_1 and k_2 are shown. Here, P1 and P2 refer to traveling wave components comprising the first and second sw pulses, and RO denotes the traveling wave read-out pulse sent along k_1. Both AWGs and the PLL are externally referenced to a 10-MHz Rb clock.

down in order to reduce heating due to photon scattering. With this procedure we achieve temperatures as low as $\mathcal{T} = 2.4\,\mu$K.

Light from the Ti:sapphire laser is also used to derive the AI pulses. A "gate" AOM operating in dual-pass configuration shifts the undiffracted light from the "trapping" AOM from $\nu_L = \nu_0 + 130$ MHz to $\nu_L = \nu_0 + 290$ MHz. The gate AOM is also pulsed so as to serve as a high-speed shutter during the experiment. The light from the gate AOM is split and sent into two separate AOMs (referred to as the "k_1" and "k_2" AOMs) operating at 240 MHz $\pm\, \delta(t)$ that produce the sw pulses. Here, $\delta(t) = gt/\lambda$ is a time-dependent frequency shift that is added to (subtracted from) the radio frequency (rf) driving the k_1 (k_2) AOM using an arbitrary waveform generator, as shown in Fig. 4. Chirping the excitation pulses in this manner cancels the Doppler shift of the atoms falling under gravity. The rf driving these AOMs is also phase locked to a 10-MHz rubidium clock to eliminate any electronically induced phase shifts. Light entering the k_1 AOM is downshifted by 240 MHz + $\delta(t)$ and sent into an optical fiber that carries the light toward the MOT. Similarly, the k_2 AOM downshifts the light by 240 MHz − $\delta(t)$. In this configuration, the detuning of the k_1 (k_2) pulse is $\Delta_1 = 50$ MHz − $\delta(t)$ [$\Delta_2 = 50$ MHz + $\delta(t)$]. This light is coupled into a separate fiber and aligned through the MOT along the vertical direction, as illustrated in Fig. 3. The output of both fibers is expanded to a e^{-2} diameter of ∼2 cm. The rf pulses driving the k_1 and k_2 AOMs are controlled using TTL switches with an isolation ratio of 100 dB, which produces optical pulses with rise times of ∼20 ns. The "gate" AOM is turned off between excitation pulses to further reduce background light from reaching the atoms.

In the vicinity of any given echo (see Fig. 1), the read-out pulse is applied to the sample along the k_1 direction and a coherent back-scattered field from the atoms occurs along the

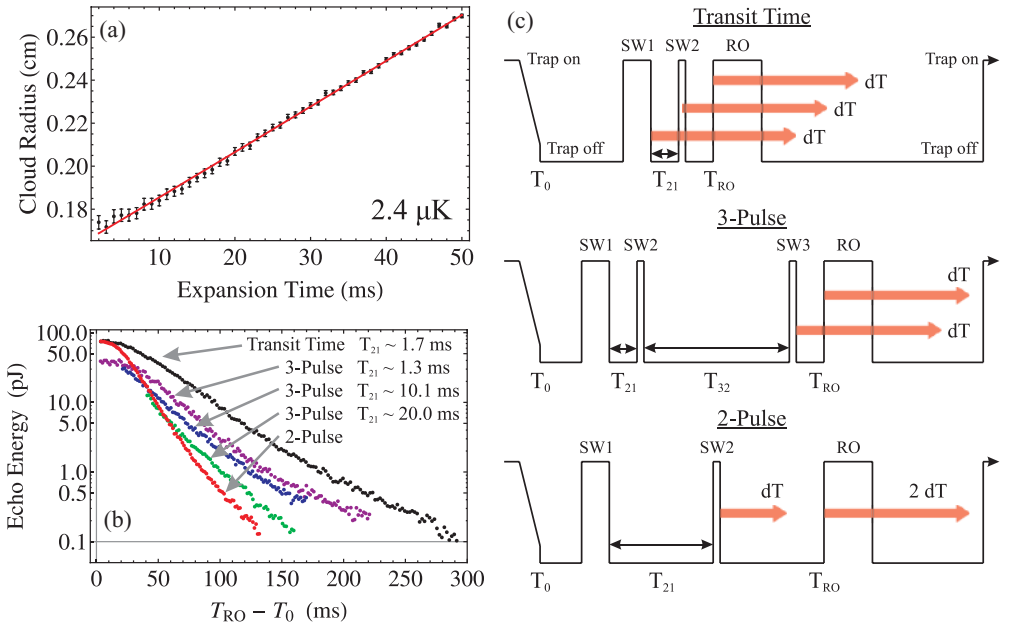

FIG. 5. (Color online) (a) Temperature measurement of the laser-cooled sample. The horizontal e^{-1} cloud radius is measured as a function of expansion time using a CCD camera. A hyperbolic fit to these data (shown as the solid red line) yields a measurement of $\mathcal{T} = 2.4 \pm 0.2\ \mu$K. Each error bar is the 1σ statistical uncertainty of the cloud radius obtained from a Gaussian fit to each cloud profile. (b) Data showing the signal lifetime for various pulse configurations. The horizontal axis is the time of the read-out pulse $T_{\rm RO}$, relative to the time of trap turn-off T_0, which signifies the start of the experiment. An echo energy of ~ 0.1 pJ is equivalent to the level of noise in the detector. These data were obtained with pulse durations for the two-pulse (three-pulse) AI: $\tau_1 = 800$ (800) ns, $\tau_2 = 100$ (70) ns, $\tau_3 = 0$ (70) ns; pulse intensity $I \sim 64$ mW/cm^2; and a sample temperature of $\mathcal{T} \sim 20\ \mu$K. Pulse separations for each configuration are shown in the figure. (c) Pulse timing diagrams for the data shown in (b). The red arrows distinguish which pulses were varied and the time step dT indicates the amount each pulse was incremented relative to the others. For the two-pulse AI, $dT = n\tau_q$, where $n = 10$. Pulses without arrows are fixed in time.

direction of $\boldsymbol{k}_2$. The power of the scattered field is recorded as a function of time using a photomultiplier tube (PMT) that is gated on for 9 μs. The echo signal lasts $\tau_{\rm coh} \sim 3\ \mu$s before coherence is lost due to Doppler dephasing. For $T_{21} \leqslant 10$ ms, the scattered field can reach powers greater than 100 μW. However, for $T_{21} > 10$ ms, the signal size decreases exponentially. The noise floor for the PMT is approximately 0.1 μW. Typically, one computes the time-integrated area of the echo signal as a measure of the signal size for a given set of parameters. Since this quantity has units of energy, it is henceforth referred to as the echo energy.

IV. RESULTS AND DISCUSSION

We now review the main experimental results of this work relating to long-lived AI signals and sensing externally applied B gradients.

A. Investigations of AI time scale

Figure 5(a) shows a measurement of the temperature of the laser-cooled sample. At $t = T_0$, all optical and magnetic fields associated with the MOT are switched off and the atoms are allowed to thermally expand in the dark. At $t = T_0 + T_{\rm exp}$, the trapping and repump beams are turned back on and a calibrated charged-coupled device (CCD) is triggered to photograph the cloud with an exposure time of 100 μs. This process is repeated for various expansion times $T_{\rm exp}$, and the e^{-1} radius of the cloud R is measured by fitting to the Gaussian intensity profiles obtained from each image. The temperature is obtained by fitting to a hyperbola [32,33] with the form $R = [R_0^2 + \sigma_v^2 (T_{\rm exp} - t_0)^2]^{1/2}$, where R_0 is the initial cloud radius, $\sigma_v = (2k_B\mathcal{T}/M)^{1/2}$ is the e^{-1} radius of the velocity distribution, and t_0 is a phenomenological offset from $T_{\rm exp} = 0$. The data shown in Fig. 5(a) give a temperature of $\mathcal{T} \sim 2.4(2)\ \mu$K in ^{85}Rb. This relatively low MOT temperature is attributed to the well-controlled magnetic environment within the glass cell, as well as the molasses cooling procedure described above.

Measurements of the AI signal lifetime under different pulse configurations are shown in Fig. 5(b), with each configuration explained schematically in Fig. 5(c). For the transit time measurement, the two-pulse AI configuration was used with T_{21} fixed. The excitation and read-out pulses were incremented synchronously. The signal lifetime for the three-pulse AI was determined by fixing T_{21} and varying the third sw pulse and read-out synchronously. For the two-pulse AI, the lifetime was measured by fixing the first sw pulse and incrementing the second sw pulse and read-out in steps $n\tau_q$ and $2n\tau_q$, respectively, where $n = 10$.

Here, all ambient B fields and B gradients are canceled along all three axes at the level of $\sim$1 mG and $\sim$0.1 mG/cm, respectively. The transit time data were obtained by using the two-pulse AI with T_{21} fixed at $\sim$1.690 ms and varying the time of all sw pulses relative to the time of trap turn-off T_0. In this measurement, the AI signal is proportional to the number of atoms that remain in the volume defined by the $\sim$2-cm

diameter excitation beams during the thermal expansion of the cloud. Although the echo energy spans almost three orders of magnitude as it decays exponentially, signals are clearly distinguishable from the noise floor (∼0.1 pJ) at times as large as ∼270 ms, as shown in Fig. 5(b). This time represents the transit time limit for the conditions of our experiment—corresponding to a drop height of ∼36 cm. This distance nearly coincides with the bottom viewport of the vacuum system. We emphasize here that such lifetimes are not possible with this interferometer unless the frequencies of the $\boldsymbol{k}_1$ and $\boldsymbol{k}_2$ beams are oppositely chirped such that the Doppler shift due to gravity [$\delta(t) = gt/\lambda$] is canceled *or* the bandwidth of the sw pulses is large enough to account for such a shift. The frequency chirp puts the sw pulses on resonance for the two-photon transition back to the same ground state for all times during the sample's free fall.

The signal lifetime for the two-pulse AI configuration is shown as the red curve in Fig. 5(b). Here, the signal lasts approximately 130 ms, corresponding to $T_{21} \sim 65$ ms. To the best of our knowledge, this is the largest time scale observed with the two-pulse configuration of this interferometer, corresponding to more than a factor of 6 improvement over our previous work [15,23,24,26]. However, the lifetime of the two-pulse echo is still limited by decoherence from a small, inhomogeneous B gradient that the atoms sample over the ∼8 cm they have fallen in 130 ms. A nonlinear $B(z)$ produces a spatially dependent force between interfering trajectories—resulting in a differential phase shift between paths of the interferometer that causes dephasing and, therefore, a loss of signal. Such a nonlinearity in $B(z)$ has been measured to be $\partial^2 B/\partial z^2 \sim -0.4$ mG/cm^2 with a flux-gate magnetometer placed at different spatial locations around the glass chamber. This curvature is produced by a combination of nonideal coil configurations and the presence of nearby ferromagnetic materials.

There are two important features that should be recognized from the data for the three-pulse AI shown in Fig. 5(b). First, at $T_{\mathrm{RO}} - T_0 \approx 0$, the echo energy for the three-pulse AI is a factor of ∼2 smaller than that of the two-pulse AI. This comes about because the additional Kapitza-Dirac pulse involved in the three-pulse AI produces fewer pathways that result in interference at the echo time compared to the two-pulse AI. Second, the lifetime of the three-pulse echo depends strongly on the value of T_{21}. As T_{21} increases, the signal lifetime approaches that of the two-pulse AI. This feature comes about because, between the second and third sw pulses, the wave packets that interfere at the echo times have a constant spatial separation [see Fig. 1(b)], which is given by $\Delta z = \bar{N}\hbar q T_{21}/M$. From this expression, it is clear that Δz can be controlled by T_{21} and the choice of echo order $\bar{N}$. By decreasing this separation, the interferometer becomes less sensitive to decoherence from nonlinear B fields since phase shifts produced by this effect become approximately common mode between interfering momentum states. Reference [14] also used this interferometer and a magnetic guide to show that smaller spatial separations lead to increased time scales.

In general, the lifetime for the three-pulse echo can be tailored to last much longer than that of the two-pulse echo, which is advantageous for precisely measuring the effects of external forces. For example, we achieve time scales as large as ∼220 ms for T_{21} fixed at ∼1.3 ms—which is much closer to the transit time limit than the lifetime of the two-pulse echo. To the best of our knowledge, the only experiment that has achieved longer time scales for the three-pulse AI have employed magnetic guides [14] to limit transverse expansion of the sample and thereby extending the transit time.

B. Investigations of external B gradients

When T_{21} is large, the two-pulse AI can be used to explore the sensitivity to small external B gradients. We demonstrate the detection of changes in the B gradient as small as $\sim 4 \times 10^{-5}$ G/cm in Fig. 6(a). Here, the $\bar{N} = 1$ echo signal was recorded with T_{21} fixed at ∼40.6 ms for various applied gradients. Changes in the gradient were facilitated by varying the current through the set of vertical quadrupole coils centered on the MOT (see Fig. 3). The smallest controllable increment in current we could achieve was 1 mA, which corresponds to a change of ∼0.04 mG/cm as estimated from an independent calibration based on a flux-gate magnetometer.

In a similar experiment, the $\bar{N} = 1$ echo energy was measured for T_{21} fixed at ∼40.6 ms as a function of β, as shown in Fig. 6(b). Here, it is clear that the echo energy has a strong periodic dependence on the applied B gradient. These data provide confirmation of the theoretical prediction given by Eqs. (7) and (8). This dependence is produced by the interference between electric fields scattered off of gratings produced by different magnetic sublevels. For example, for

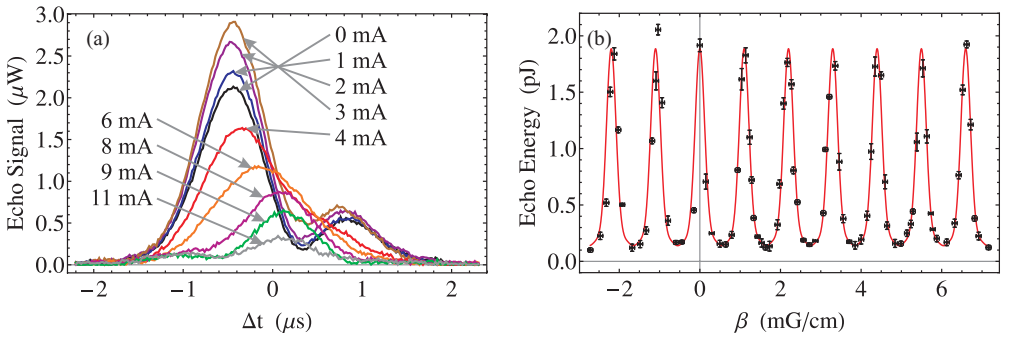

FIG. 6. (Color online) (a) First order ($\bar{N} = 1$) two-pulse echo signal for various applied B-field gradients β. The theoretically expected echo time is at $\Delta t = t - 2T_{21} = 0$. Each mA of current corresponds to a change of ∼0.04 mG/cm in the applied gradient. (b) First order ($\bar{N} = 1$) two-pulse echo energy as a function of β. The solid red line is a fit based on Eq. (12). The value of β is obtained from a calibration using a flux-gate magnetometer. Pulse parameters for both (a) and (b): $\tau_1 = 800$ ns, $\tau_2 = 130$ ns, I∼64 mW/cm^2, $T_{21} \sim 40.6$ ms.

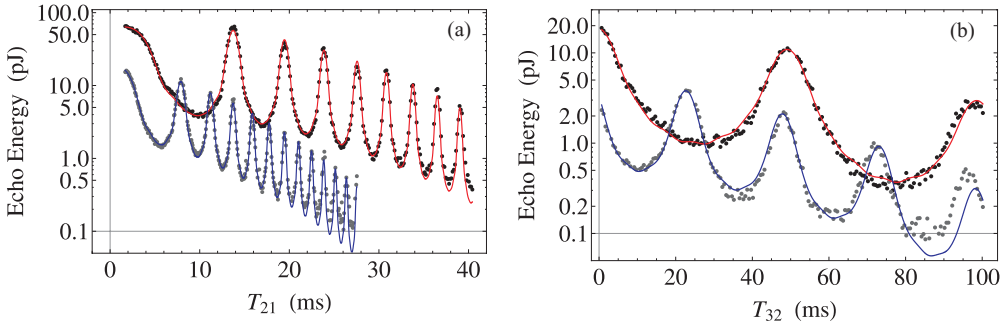

FIG. 7. (Color online) (a) Two-pulse echo energy as a function of T_{21} in the presence of a fixed β. Gradient-induced oscillations are shown for the first two echo orders (black points, $\bar{N} = 1$; gray points, $\bar{N} = 2$). Here, T_{21} is varied in integer multiples of τ_q to avoid sensitivity to atomic recoil effects. Fits based on Eq. (12), shown as the solid lines, give $|\beta| = 9.30(1)$ mG/cm and $|\beta| = 9.34(1)$ mG/cm, respectively. (b) Data analogous to (a) obtained using a slightly larger gradient with the three-pulse AI. Here, T_{21} is fixed at 2.0 ms and T_{32} is varied to map out the modulation for the first two echo orders (black points, $\bar{N} = 1$; gray points, $\bar{N} = 2$). Fits based on Eq. (13) give $|\beta| = 17.50(4)$ mG/cm and $|\beta| = 17.78(5)$ mG/cm, respectively. Two-pulse (three-pulse) AI parameters: $\tau_1 = 800$ (800) ns; $\tau_2 = 100$ (70) ns; $\tau_3 = 0$ (70) ns; $I \sim 64$ mW/cm^2.

a given β, gratings produced by states $|F\, m_F\rangle$ and $|F\, m'_F\rangle$ undergo phase shifts $m_F\phi_\beta^{(2)}$ and $m'_F\phi_\beta^{(2)}$, respectively, where $\phi_\beta^{(2)}$ is given by Eq. (8). For constructive interference between fields scattered by these states, the B gradient must satisfy $(m_F - m'_F)\phi_\beta^{(2)}/2 = 2n\pi$, for integer n. Thus, as β is varied, the phase shift induced in the $|F\, m_F\rangle$ and $|F\, m'_F\rangle$ gratings produces periodic constructive (destructive) interference in the total scattered field, and therefore, maxima (minima) in the echo energy. This process occurs simultaneously in all $2F + 1$ sublevels. As a result, the observed signal is a weighted sum of the scattered fields from all states. Here, there are $2F(2F + 1) = 42$ pairs of states that produce interference—although not all pairs have unique contributions. Since the excitation beams were circularly polarized in the experiment, the fields scattered from the extreme states ($|3\,3\rangle$ or $|3\,{-3}\rangle$) dominate the signal.

We use the following model, based on the squared modulus of Eq. (7), to fit the data shown in Fig. 6(b):

$$S^{(2)}(\beta, T_{21}) = S_0 e^{-(T_{21}-t_0)^2/\tau^2} \sum_{m_F, m'_F} a_{m_F} a_{m'_F} \times e^{iA(m_F - m'_F)\beta\bar{N}(\bar{N}+1)(T_{21}-t_1)^2}, \quad (12)$$

where S_0, t_1 and the set of $\{a_{m_F}\}$ are free parameters, $A = qg_F\mu_B/2M$ is a constant, and t_0 was set to T_{21} for this data. In this model, the Gaussian factor outside the sum is added phenomenologically to account for signal loss due to both the transit time and any decoherence in the system. In addition, each a_{m_F} is proportional to the magnetic sublevel population, $|\alpha_{m_F}|^2$, through Eq. (A21). As a result, these parameters are constrained to be positive. All other fit parameters are unconstrained. In principle, it should be possible to obtain the sublevel populations from the set of best fit parameters $\{a_{m_F}\}$. However, determining the constant of proportionality between the a_{m_F}, the populations, and the scattered field intensity is complicated [34,35] and not addressed by the theory presented here. We emphasize, however, that fits to data presented in this work give similar results for the set of $\{a_{m_F}\}$, which are consistent with our expectations for circularly polarized excitation beams.

Surveys of gradient-induced modulation on the echo signal shown in Fig. 7 provide additional confirmation of the theory outlined in Sec. II and the Appendix. Figure 7(a) indicates that, in the presence of a B gradient, the two-pulse echo energy becomes modulated at a frequency that increases linearly with T_{21} (i.e., the modulation is chirped), as predicted by Eq. (9). This figure shows gradient oscillations for both the $\bar{N} = 1$ and the $\bar{N} = 2$ orders of the two-pulse echo. Since the chirp rate increases as $\bar{N}(\bar{N} + 1)$, the second-order echo is modulated at a rate three times that of the first-order echo. Confirmation of this is provided by a least-squares fit to the data based on Eq. (12), as shown by the solid lines in Fig. 7(a). Since the gradient was held fixed in the experiment, the fits to the two data sets should provide similar measurements of $|\beta|$.[1] The two measurements yield $|\beta| = 9.30(1)$ mG/cm for $\bar{N} = 1$ and $|\beta| = 9.34(1)$ mG/cm for $\bar{N} = 2$, where the quoted error is the 1σ statistical uncertainty generated by the fit. These measurements are in good agreement with each other and an independent measurement from a flux-gate magnetometer. We emphasize that accurate fits to these data and the extraction of β were possible only through the development of the multilevel formalism presented in the Appendix. In particular, since the oscillations shown in Fig. 7(a) do not occur with 100% contrast (i.e., each oscillation minima does not reach the level of the noise), a model including only two magnetic sublevels with equal excitation probabilities, such as that described in Ref. [26], is insufficient to model the data.

Figure 7(b) shows data similar to that shown in Fig. 7(a), but for the first two orders of the three-pulse echo and a slightly larger B gradient. These data illustrate that the three-pulse AI is less sensitive to gradients than the two-pulse AI. Since T_{21} is fixed at 2.0 ms, the modulation frequency is constant

[1]Measurements of the B gradient from the scattered field intensity are not sensitive to the sign of β. However, the sign can be determined using a heterodyne technique to measure the scattered electric field amplitude.

and proportional to $\bar{N}$ and T_{21}—confirming the predictions of Eq. (11). The data are fit to the following model:

$$S^{(3)}(\beta, T_{32}, T_{21}) = S_0 e^{-(T_{32}-t_0)^2/\tau^2} \sum_{m_F, m'_F} a_{m_F} a_{m'_F} \times e^{iA(m_F - m'_F)\beta[\bar{N}(\bar{N}+1)T_{21}^2 + 2\bar{N}T_{21}(T_{32}-t_1)]}, \quad (13)$$

which is based on Eqs. (A25), (A26), and (A28), with a Gaussian decay factor added phenomenologically. All other parameters in this model are similar to those discussed in reference to Eq. (12). Measurements of the magnitude of the gradient from fits to these data yield $|\beta| = 17.50(4)$ mG/cm and $|\beta| = 17.78(5)$ mG/cm for the $\bar{N} = 1$ and $\bar{N} = 2$ echoes, respectively. These two measurements differ by more than 5σ, which deserves some explanation. By inspecting the fit to the $\bar{N} = 2$ echo, it is clear that the data are not well modeled by a single frequency sinusoid as T_{32} becomes large. This provides evidence that the atoms are sampling different gradients as they drop under gravity—an effect that is not accounted for in the theory. By analyzing different sections of these data, we estimate that the gradient varies by as much as ∼1.6 mG/cm between $T_{32} \sim 40$ ms and 100 ms—during which time atoms fall ∼4 cm. Independent measurements of the curvature of the B field, where $|\beta|$ was found to change by ∼0.4 mG/cm every centimeter, are consistent with the variation in β detected by atoms.

Although we have demonstrated sensitivity to *changes* in the B gradient as small as $\sim 4 \times 10^{-5}$ G/cm using $T_{21} \sim 40$ ms with the two-pulse AI, our ability to measure the absolute magnitude of the applied gradient is less sensitive. This is primarily because the measurement is based on fitting data to an oscillatory model and extracting the modulation rate—which cannot be done accurately without the presence of an oscillatory component in the data. To estimate the smallest measurable B gradient with the two interferometers, we tuned the applied fields for each AI separately such that the first revival in the $\bar{N} = 1$ echo energy occurred at the largest time. The resulting data are shown in Fig. 8, which yielded measurements of $|\beta| = 0.26(3)$ mG/cm for the two-pulse AI [Fig. 8(a)] and $|\beta| = 9.5(1)$ mG/cm for the three-pulse AI [Fig. 8(b)].

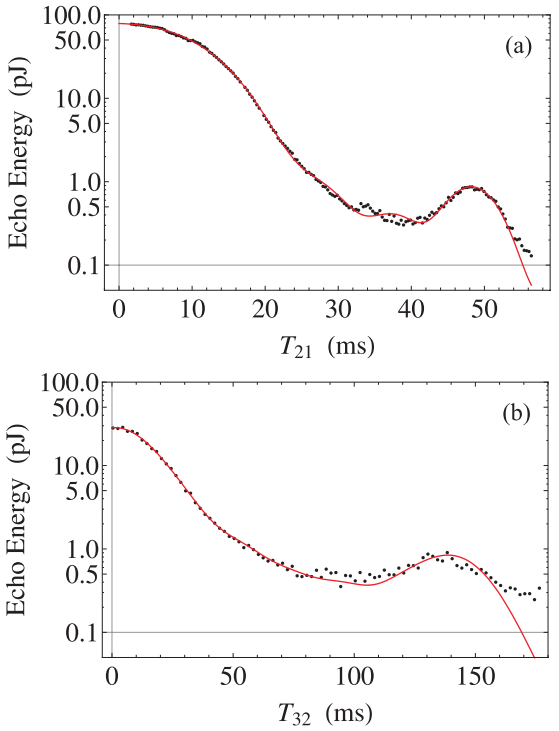

FIG. 8. (Color online) Smallest direct measurement of a B gradient using the two-pulse (a) and three-pulse (b) AIs. Here, the applied fields were tuned separately for each AI such that the first revival in the $\bar{N} = 1$ echo energy occurred at the largest time. A fit based on Eq. (12) for the two-pulse AI gave $|\beta| = 0.26(3)$ mG/cm. Similarly, a fit based on Eq. (13) yielded $|\beta| = 9.5(1)$ mG/cm for the three-pulse AI, with $T_{21} \sim 1.27$ ms. Two-pulse (three-pulse) AI parameters: $\tau_1 = 800$ (800) ns, $\tau_2 = 100$ (70) ns, $\tau_3 = 0$ (70) ns, $I \sim 64$ mW/cm^2.

V. APPLICATIONS TO GRAVITY

The apparatus shown in Fig. 3 is not isolated from external vibrations and is unsuitable for measurements of the optical phase of the scattered read-out light using heterodyne detection. For this reason, a measurement of g from the phase of the atomic grating [21,26] is beyond the scope of this article and will be presented elsewhere. However, the aforementioned results relating to B gradients validate theoretical predictions that can be applied to precise measurements of gravity. In this section, we discuss the feasibility of such a measurement by applying the formalism presented in the Appendix.

The best portable gravimeter [36] uses an optical Mach-Zehnder interferometer where one arm contains a free-falling corner cube for position-sensitive measurements of g at the level of ∼1 ppb over a few minutes. The position sensitivity in these devices comes from detecting interference fringes as a function of the drop time of the cube relative to an inertial frame defined by a stationary mirror. The frequency at which the fringes accumulate scales linearly with the drop time (i.e., the frequency is chirped). The matter-wave analog of this gravimeter is the two-pulse grating echo AI [21,26], where changes in the phase of the grating due to gravity are detected relative to the nodes of an sw—which serves as the inertial reference frame. In this case, the accumulation of fringes due to matter-wave interference is also described by a chirped-frequency sinusoid.

We now review the main results of the grating echo theory that pertain to gravity. The gravitational potential can be written as

$$\hat{U}(z) = Mg\hat{I}z, \quad (14)$$

where the force is $\mathcal{F} = -Mg$ and $\hat{I}$ is the $(2F+1) \times (2F+1)$ identity matrix. The effect on the AI is similar to that of the B gradient on a sample that has been optically pumped into a single state. Since gravity acts equally on all states, the phase shift of the grating produced by each state is the same. Therefore, the expression for the field

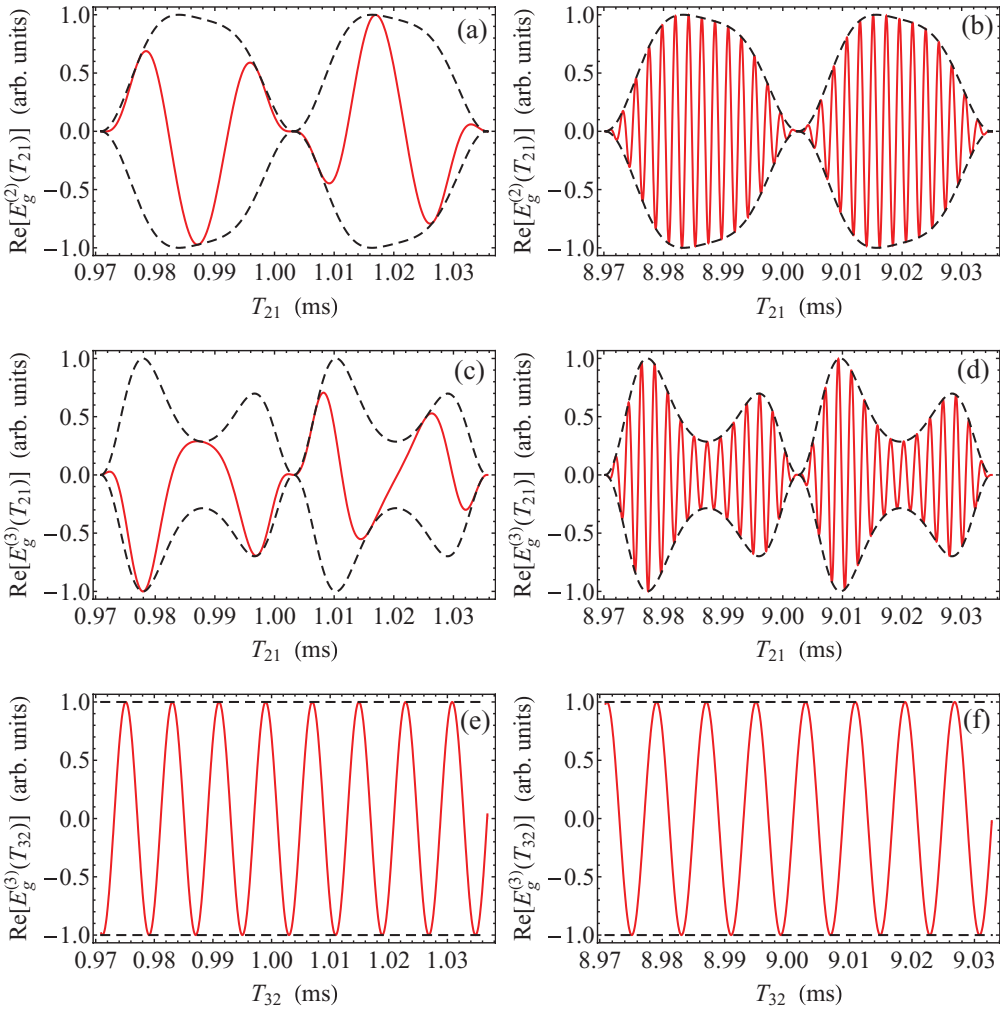

FIG. 9. (Color online) The real part of the scattered electric field (red solid line) in the presence of gravity for the two-pulse (a) and (b) and the three-pulse (c)–(f) AIs. In parts (a)–(d), the black dashed line shows the signal envelope [based on Eq. (A21) for (a) and (b) and Eq. (A29) for (c) and (d)], which is modulated at $2\omega_q \approx 2\pi \times 31$ kHz. (a) The field oscillates at a frequency $\omega_g^{(2)}(T_{21}) \sim 2\pi \times 50$ kHz in the vicinity of $T_{21} \sim 1$ ms. (b) The modulation frequency increases to $\omega_g^{(2)} \sim 2\pi \times 450$ kHz at $T_{21} \sim 9$ ms. Parts (c) and (d) show results for the three-pulse AI as a function of T_{21}, with T_{32} fixed at 100 μs. The field oscillates at approximately the same frequency in (a) and (c), and in (b) and (d), since T_{32} is small. Parts (e) and (f) show the three-pulse signal as a function of T_{32} with $T_{21} = 5$ ms. Since T_{21} is fixed, there is no sensitivity to atomic recoil and the signal envelope is not modulated. As T_{32} increases, the modulation frequency of the scattered field amplitude remains fixed at $\omega_g^{(3)}(T_{21}) \sim 2\pi \times 125$ kHz.

scattered from the grating simplifies significantly compared to Eq. (7):

$$E_g^{(2)}(t;\boldsymbol{T}) = \left[\sum_{m_F} E_{m_F}^{(2)}(t;\boldsymbol{T})\right] e^{i\phi_g^{(2)}(t;\boldsymbol{T})}, \tag{15}$$

where the grating phase due to gravity is

$$\phi_g^{(2)}(\Delta t; T_{21}) = -\frac{qg}{2}\left\{\bar{N}(\bar{N}+1)T_{21}^2 + 2[T_1 + (\bar{N}+1)T_{21}]\Delta t + \Delta t^2\right\}, \tag{16}$$

as determined by Eq. (A23). This phase cannot be detected from the intensity of the scattered light because there is no differential phase shift between magnetic sublevels—thus, there is no amplitude modulation of the grating [26]. The scaling of the grating phase with T_{21}^2 in Eq. (16) shows the similarity between the two-pulse AI and the optical Mach-Zehnder interferometer discussed in Ref. [36].

Figures 9(a) and 9(b) show the expected two-pulse AI signal in the presence of gravity as a function of T_{21}—illustrating that the modulation frequency is chirped linearly with T_{21} ($\omega_g^{(2)} = \partial\phi_g^{(2)}/\partial T_{21} \propto T_{21}$). As T_{21} increases, $\omega_g^{(2)}$ becomes larger than the recoil frequency (for the first-order echo in ^{85}Rb, this occurs when $T_{21} > 300$ μs), and T_{21} must be incremented in steps less than τ_q to avoid undersampling the frequency. However, this effect causes reduced sensitivity to the grating phase, since modulation at the recoil frequency produces periodic regions with small signal amplitude. Additionally, as shown in Ref. [14], this AI is very sensitive to phase changes due to mirror vibrations, which can be detrimental to measurements of g using this technique.

Figures 9(c) and 9(d) show the expected three-pulse signal as a function of T_{21} in the presence of gravity. It is clear that

the envelope of the scattered field has a complicated periodic dependence on T_{21}, with a zero every $\tau_q \sim 32$ μs due to the destructive interference of momentum states differing by $\hbar q$. This is similar to the two-pulse case shown in Figs. 9(a) and 9(b). Here, the grating phase modulation frequency is given by

$$\left|\frac{\partial \phi_g^{(3)}}{\partial T_{21}}\right| = qg[\bar{N}(\bar{N}+1)T_{21} + \bar{N}T_{32} + (\bar{N}+1)\Delta t], \qquad (17)$$

which is identical to the two-pulse case, $\omega_g^{(2)}$, with the addition of the term proportional to T_{32}.

Figures 9(e) and 9(f) show the expected three-pulse signal as a function of T_{32}, with T_{21} fixed at 5 ms. In this case, there is no sensitivity to atomic recoil, so the envelope remains at a constant level as T_{32} is varied. The frequency of the phase modulation is also fixed by $\bar{N}$ and T_{21}, as given by

$$\omega_g^{(3)}(T_{21}) = \left|\frac{\partial \phi_g^{(3)}}{\partial T_{32}}\right| = qg(\bar{N}T_{21} + \Delta t). \qquad (18)$$

For the conditions presented in these figures, $\omega_g^{(3)} \sim 2\pi \times$ 125 kHz. The work of Ref. [14] shows that the three-pulse AI is significantly less sensitive to mirror vibrations than the two-pulse AI if $T_{32} \gg T_{21}$. Our results have also shown that this configuration is less sensitive to B gradients. For all these reasons, this AI is particularly well suited for precise measurements of g.

Simulations of the two-pulse AI signal with $\bar{N} = 1$, $T_{21} \sim$ 150 ms, and a phase error of 1% suggest the precision of a measurement of g should be ~1.4 ppb. Similarly, we estimate a precision of ~0.4 ppb for the three-pulse AI using $\bar{N} = 1$, $T_{21} = 75$ ms, T_{32} varied over 150 ms, and the same phase error. From these estimates, it is clear that these AIs can have greater sensitivity than the best industrial sensor [36]. Since the precision scales linearly with the phase error, we anticipate further improvements in sensitivity without extending the time scale. If systematic effects of such a cold atom gravimeter are characterized, it may be possible for the AI experiment to serve as a reference to calibrate other gravimeters.

VI. CONCLUSIONS

Measurements of applied B gradients using both the two- and three-pulse techniques are in good agreement with independent measurements of β using a flux gate magnetometer. We have demonstrated sensitivity to changes in the B gradient at the level of $\sim 4 \times 10^{-5}$ G/cm. This result is comparable to the ~300 pT/mm resolution achieved in recent experiments using a Raman AI [31]. Absolute measurements of $|\beta|$ as small as $\sim 3 \times 10^{-4}$ G/cm were also possible using the two-pulse AI. These measurements are highly dependent on an accurate description of the data presented above, which necessitates the inclusion of effects due to all ground-state magnetic sublevels. We have also shown sensitivity to spatial variation in the B gradient using a long-lived second-order ($\bar{N} = 2$) three-pulse echo. This nonlinearity in the ambient B field strongly affects the signal lifetime in grating echo AIs.

As tests of the theoretical results presented in Sec. II, we have separately confirmed the linear dependence of the β-induced oscillation frequencies, $\omega_\beta^{(2)}$ and $\omega_\beta^{(3)}$ [given by Eqs. (9) and (11), respectively], on the B gradient. We have also verified that these frequencies both scale linearly with T_{21}, and, for the three-pulse AI, $\omega_\beta^{(3)}$ is constant as a function of T_{32}.

Since we have achieved signal lifetimes approaching the transit time limit, we have shown that fountain-based experiments are possible with grating echo AIs. The advantage of a fountain configuration is that the spatial extent of the AI (~11 cm for a 300-ms time scale) can be made small, which reduces the requirements for inhomogeneous B-field suppression. Such a configuration is ideal for precise measurements of gravity, particularly with the three-pulse AI. Passive suppression of B fields with a series of cancellation coils, or optically pumping into the $m_F = 0$ sublevel, represent two ways in which such a measurement can be realized.

Despite the widespread use of Raman-type AIs for inertial sensing [8,37,38], grating echo-type AIs—which offer reduced experimental complexity—are also excellent candidates for precision measurements of ω_q and g. This work has brought about understanding of systematic effects produced by B gradients on these measurements.

In summary, we have developed an improved understanding of the effects of a constant force that applies to time-domain grating echo AIs. Although the sensitivity for AI-based gradient detection cannot compete with commercial magnetic gradiometers (which offer sensitivities of the order of ~1 pT/m), the technique is useful for absolute measurements of gradients in cold atom experiments.

ACKNOWLEDGMENTS

This work was supported by the Canada Foundation for Innovation, Ontario Innovation Trust, Natural Sciences and Engineering Research Council of Canada, Ontario Centres of Excellence, and York University. We also thank Itay Yavin of McMaster University for helpful discussions, and Adam Carew of York University for constructing phase-locked loops.

APPENDIX

In this appendix, we derive expressions for the signals generated by the two- and three-pulse interferometers in the presence of a constant external force $\mathcal{F}$. In Ref. [26], a similar calculation for the two-pulse signal is given, in which only two ground-state sublevels are considered, and effects due to spontaneous emission are ignored. Here, we account for $2F + 1$ magnetic sublevels in the field scattered from the atoms, as well as spontaneous emission during the excitation pulses. Both of these effects are crucial for an accurate description of these interferometers. We also give a general expression for the signal generated by an N-pulse AI from which all classes of time-domain grating echo AIs can be realized.

The potential is assumed to have the form $\hat{U}(z) = -\hat{\mathcal{M}}z$, where $\hat{\mathcal{M}} = -\partial\hat{U}/\partial z$ is an operator that computes with z and p, and acts on the basis states $|F\ m_F\rangle$ with eigenvalues $m_F\mathcal{F}$. Here, $\mathcal{F}$ is a constant with units of force. We proceed by computing the ground-state wave function after the application of each sw pulse at times $t = T_1$ and T_2, with a period of evolution before, between, and after each pulse (with durations

T_1, $T_2 - T_1$, and $t - T_2$, respectively) in the presence of the force. During the application of each sw pulse, the kinetic and potential energy terms in the Hamiltonian are ignored by assuming the pulses are sufficiently short such that the atom does not move significantly (Raman-Nath approximation). In this manner, the sw pulses are treated as δ-function excitations, although they are given durations τ_j for the purposes of the calculation.

The interferometer signal is defined as the back-scattered electric field amplitude at the time of an echo, which is proportional to the amplitude of the q-Fourier harmonic of the density distribution at these times. The results for the two-pulse AI signal are then generalized for an N-pulse AI, from which we compute the three-pulse AI signal.

The Hamiltonian for the ground state $|F\ m_F\rangle$ in the presence of an sw field and an external potential, $\hat{U}(z)$, can be approximated by [15,16]

$$\hat{H}_{m_F} = \frac{p^2}{2M} + \hbar\chi_{m_F} e^{i\theta}\cos(qz) + \hat{U}(z), \tag{A1}$$

where θ is a phase associated with spontaneous emission during the sw pulse,

$$\theta = \tan^{-1}\left(-\frac{\gamma}{\Delta}\right), \tag{A2}$$

and χ_{m_F} is a two-photon Rabi frequency given by

$$\chi_{m_F} = \frac{\Omega_0^2}{2\Delta}\left(1+\frac{\gamma^2}{\Delta^2}\right)^{-1/2}\left(C^{F\ \ 1\ \ F+1}_{m_F\ q_L\ m_F+q_L}\right)^2. \tag{A3}$$

Here, Ω_0 is the on-resonance Rabi frequency for a two-level atom, $\Delta = \omega_L - \omega_0$ is the atom-field detuning with atomic resonance frequency ω_0 and laser frequency ω_L, γ is half of the spontaneous emission rate, and $(C^{F\ \ 1\ \ F+1}_{m_F\ q_L\ m_F+q_L})$ is a Clebsch-Gordan coefficient for a light field with a polarization state q_L. We ignore the excited state in this treatment, since the field is assumed to be relatively weak and far off-resonance ($|\Delta| \gg \Omega_0, \gamma$). We also neglect the Zeeman shift of magnetic sublevels by assuming $|\Delta| \gg g_F\mu_B B/\hbar$.

The amplitude of the ground-state wave function at $t = 0$ can be written as a superposition of spin states:

$$a(z,0) = \sum_{m_F} a_{m_F}(z,0)\,|F\ m_F\rangle\,, \tag{A4}$$

where the amplitude of each spin state is

$$a_{m_F}(z,0) = \frac{\alpha_{m_F}}{\sqrt{2\pi\hbar}} e^{ip_0 z/\hbar}, \tag{A5a}$$

$$a_{m_F}(p,0) = \alpha_{m_F}\delta(p - p_0). \tag{A5b}$$

Here, p_0 is the initial momentum of the atom along the z direction, $|\alpha_{m_F}|^2$ is the population of state $|F\ m_F\rangle$, with $\sum_{m_F}|\alpha_{m_F}|^2 = 1$, and $a_{m_F}(p,0)$ is the amplitude of the spin state in momentum space.

The main challenge in this calculation is evolving the wave function between sw pulses in the presence of the additional potential energy $\hat{U}(z)$. In the absence of this potential, it is straightforward to integrate the Schrödinger equation in momentum space. However, with $\hat{U}(z)$ present, we have the following equation of motion:

$$i\hbar\frac{\partial a_{m_F}}{\partial t} = \left(\frac{p^2}{2M} - \hat{\mathcal{M}}z\right)a_{m_F}(p,t). \tag{A6}$$

One can integrate this equation to find

$$a_{m_F}(p,t) = e^{-i(-\hat{\mathcal{M}}z + p^2/2M)t/\hbar}a_{m_F}(p,0), \tag{A7}$$

but some care must be taken when evaluating the right-hand side. The challenge arises from the fact that z and $p = -i\hbar\partial/\partial z$ are noncommuting operators. As a result, the exponential in Eq. (A7) is really a matrix exponential of noncommuting matrices $\hat{A}$ and $\hat{B}$. In general $e^{\hat{A}+\hat{B}} \neq e^{\hat{A}}e^{\hat{B}}$, but one can use the Zassenhaus formula [39] to expand the matrix exponential as

$$e^{\xi(\hat{A}+\hat{B})} = e^{\xi\hat{A}}e^{\xi\hat{B}}e^{-\xi^2[\hat{A},\hat{B}]/2} \times e^{\xi^3(\lfloor\hat{A},[\hat{A},\hat{B}]\rfloor - 2\lfloor[\hat{A},\hat{B}],\hat{B}\rfloor)/6}\cdots, \tag{A8}$$

where ξ is an arbitrary constant. The higher order factors (represented by $\cdots$ in the above equation) vanish if $\lfloor[\hat{A},\hat{B}],\hat{B}\rfloor$ and $\lfloor\hat{A},[\hat{A},\hat{B}]\rfloor$ commute with all higher order nested commutators. Choosing $\hat{A} = -\hat{\mathcal{M}}z$ and $\hat{B} = p^2/2M$,[2] and using the commutation relations $[z,p^2] = i2\hbar p$, $[z,p] = i\hbar$, we find

$$\left[-\hat{\mathcal{M}}z, \frac{p^2}{2M}\right] = -i\frac{\hbar\hat{\mathcal{M}}}{M}p, \tag{A9a}$$

$$\left[-\hat{\mathcal{M}}z, \left[-\hat{\mathcal{M}}z, \frac{p^2}{2M}\right]\right] = -\frac{\hbar^2\hat{\mathcal{M}}^2}{M}, \tag{A9b}$$

$$\left[\left[\frac{p^2}{2M}, -\hat{\mathcal{M}}z\right], \frac{p^2}{2M}\right] = 0. \tag{A9c}$$

Using Eq. (A8) with $\xi = -it/\hbar$ and the commutators in Eqs. (A9), Eq. (A7) becomes

$$a_{m_F}(p,t) = e^{i\hat{\mathcal{M}}tz/\hbar}e^{-ip^2t/2M\hbar}e^{-i\hat{\mathcal{M}}pt^2/2M\hbar} \times e^{-i\hat{\mathcal{M}}^2t^3/6M\hbar}a_{m_F}(p,0). \tag{A10}$$

Since $e^{\xi(\hat{\mathcal{M}})^n}|F\ m_F\rangle = e^{\xi(m_F\mathcal{F})^n}|F\ m_F\rangle$, it follows that the amplitude of the state $|F\ m_F\rangle$ before the onset of the first sw pulse is

$$a_{m_F}(p,t) = \alpha_{m_F}e^{i(m_F\mathcal{F})tz/\hbar}e^{-ip^2t/2M\hbar}e^{-i(m_F\mathcal{F})pt^2/2M\hbar} \times e^{-i(m_F\mathcal{F})^2t^3/6M\hbar}\delta(p - p_0), \tag{A11a}$$

$$a_{m_F}(z,t) = \frac{\alpha_{m_F}}{\sqrt{2\pi\hbar}}e^{i(p_0+m_F\mathcal{F}t)z/\hbar}e^{-i\epsilon_0 t/\hbar}e^{-i(m_F\mathcal{F})p_0t^2/2M\hbar} \times e^{-i(m_F\mathcal{F})^2t^3/6M\hbar}, \tag{A11b}$$

where $\epsilon_0 = p_0^2/2M$ is the initial kinetic energy of the atom.

The first sw pulse, applied at $t = T_1$, diffracts the atom into a superposition of momentum states. The wave function is computed in position space using the Raman-Nath approximation and integrating the Schrödinger equation to obtain

[2]This choice is not arbitrary. Since the p-space wave function is an eigenstate of the operator $p^2/2M$, but not $-\hat{\mathcal{M}}z$, we save ourselves some effort by choosing $\hat{B} = p^2/2M$ since $e^{\hat{B}}$ operates on the wave function before $e^{\hat{A}}$.

$$a^{(1)}_{m_F}(z,T_1) = a_{m_F}(z,T_1)\sum_n (-i)^n J_n(\Theta^{(1)}_{m_F})e^{inqz}, \tag{A12a}$$

$$a^{(1)}_{m_F}(p,T_1) = \alpha_{m_F} e^{-i\epsilon_0 T_1/\hbar} e^{-i(m_F\mathcal{F})p_0 T_1^2/2M\hbar} e^{-i(m_F\mathcal{F})^2 T_1^3/6M\hbar} \sum_n (-i)^n J_n\left(\Theta^{(1)}_{m_F}\right)\delta(p - p_0 - m_F\mathcal{F}T_1 - n\hbar q). \tag{A12b}$$

Here, $\Theta^{(1)}_{m_F} \equiv u^{(1)}_{m_F} e^{i\theta}$ is the (complex) area of pulse 1, $u^{(1)}_{m_F} = \chi_{m_F}\tau_1$, τ_1 is the duration of the pulse, and $a^{(1)}_{m_F}(p,T_1)$ is the wave function in momentum space. The superscript (1) on $a^{(1)}_{m_F}$ denotes the number of sw pulses that have been applied to the atom so far. We use the prescription of Eq. (A10) to evolve the amplitude in momentum space [Eq. (A12b)] until the onset of the second pulse,

$$\begin{aligned} a^{(1)}_{m_F}(p,t) = {} & \alpha_{m_F} e^{i(m_F\mathcal{F})(t-T_1)z/\hbar} e^{-i[p_0^2 T_1 + p^2(t-T_1)]/2M\hbar} e^{-i(m_F\mathcal{F})[p_0 T_1^2 + p(t-T_1)^2]/2M\hbar} \\ & \times e^{-i(m_F\mathcal{F})^2[T_1^3 + (t-T_1)^3]/6M\hbar} \sum_n (-i)^n J_n\left(\Theta^{(1)}_{m_F}\right)\delta(p - p_0 - m_F\mathcal{F}T_1 - n\hbar q). \end{aligned} \tag{A13}$$

To apply the next sw pulse to the wave function, it is convenient to transform back to position space:

$$\begin{aligned} a^{(1)}_{m_F}(z,t) = {} & \frac{\alpha_{m_F}}{\sqrt{2\pi\hbar}} e^{i(p_0 + m_F\mathcal{F}t)z/\hbar} e^{-i[p_0^2 T_1 + (p_0 - m_F\mathcal{F}T_1)^2(t-T_1)]/2M\hbar} \\ & \times e^{-i(m_F\mathcal{F})[p_0 T_1^2 + (p_0 + m_F\mathcal{F}T_1)(t-T_1)^2]/2M\hbar} e^{-i(m_F\mathcal{F})^2[T_1^3 + (t-T_1)^3]/6M\hbar} \\ & \times \sum_n (-i)^n J_n\left(\Theta^{(1)}_{m_F}\right) e^{inqz} e^{-inqv_0(t-T_1)} e^{-in^2\omega_q(t-T_1)} e^{-inq(m_F\mathcal{F})[(t-T_1)^2 + 2T_1(t-T_1)]/2M}. \end{aligned} \tag{A14}$$

Here, $v_0 = p_0/M$ is the initial velocity of the atom and $\omega_q = \hbar q^2/2M$ is the two-photon recoil frequency. Applying the second pulse at $t = T_2$, the wave function becomes

$$\begin{aligned} a^{(2)}_{m_F}(z,T_2) = {} & \frac{\alpha_{m_F}}{\sqrt{2\pi\hbar}} e^{i(p_0 + m_F\mathcal{F}T_2)z/\hbar} e^{-i\epsilon_0^2 T_2/\hbar} e^{-ip_0(m_F\mathcal{F})T_2^2/2M\hbar} e^{-i(m_F\mathcal{F})^2 T_2^3/6M\hbar} \\ & \times \sum_{n,m} (-i)^{(n+m)} J_n(\Theta^{(1)}_{m_F}) J_m(\Theta^{(2)}_{m_F}) e^{i(n+m)qz} e^{-inqv_0(T_2-T_1)} e^{-in^2\omega_q(T_2-T_1)} e^{-inq(m_F\mathcal{F})(T_2^2 - T_1^2)/2M}. \end{aligned} \tag{A15}$$

To evolve the wave function in the presence of the external force until time t, once again we transform into p space and use Eq. (A10) to obtain

$$\begin{aligned} a^{(2)}_{m_F}(p,t) = {} & \alpha_{m_F} e^{i(m_F\mathcal{F})(t-T_2)z/\hbar} e^{-i[p_0^2 T_2 + p^2(t-T_2)]/2M\hbar} e^{-i(m_F\mathcal{F})[p_0 T_2^2 + p(t-T_2)^2]/2M\hbar} e^{-i(m_F\mathcal{F})^2[T_2^3 + (t-T_2)^3]/6M\hbar} \\ & \times \sum_{n,m} (-i)^{(n+m)} J_n\left(\Theta^{(1)}_{m_F}\right) J_m\left(\Theta^{(2)}_{m_F}\right) e^{-inqv_0(T_2-T_1)} e^{-in^2\omega_q(T_2-T_1)} e^{-inq(m_F\mathcal{F})(T_2^2 - T_1^2)/2M} \\ & \times \delta[p - p_0 - m_F\mathcal{F}T_2 - (n+m)\hbar q]. \end{aligned} \tag{A16}$$

Finally, the amplitude in position space after the second pulse can be shown to be

$$\begin{aligned} a^{(2)}_{m_F}(z,t) = {} & \frac{\alpha_{m_F}}{\sqrt{2\pi\hbar}} e^{i(p_0 + m_F\mathcal{F}t)z/\hbar} e^{-i\epsilon_0 t/\hbar} e^{-i(m_F\mathcal{F})p_0 t^2/2M\hbar} e^{-i(m_F\mathcal{F})^2 t^3/6M\hbar} \\ & \times \sum_{n,m} (-i)^{(n+m)} J_n\left(\Theta^{(1)}_{m_F}\right) J_m\left(\Theta^{(2)}_{m_F}\right) e^{i(n+m)qz} e^{-iqv_0[n(T_2-T_1) + (n+m)(t-T_2)]} \\ & \times e^{-i\omega_q[n^2(T_2-T_1) + (n+m)^2(t-T_2)]} e^{-iq(m_F\mathcal{F})[n(T_2^2 - T_1^2) + (n+m)(t^2 - T_2^2)]/2M}. \end{aligned} \tag{A17}$$

To compute the field scattered from the atomic interference as a function of t, we use the q-Fourier component of the ground-state density, $\rho^{(2)}_{m_F m_F}(z,t) = |a^{(2)}_{m_F}(z,t)|^2$, which can be shown to be

$$\begin{aligned} \rho^{(2)}_{m_F m_F}(z,t) = {} & \frac{|\alpha_{m_F}|^2}{2\pi\hbar} \sum_{n,m,n',m'} (-i)^{n+m-n'-m'} J_n\left(\Theta^{(1)}_{m_F}\right) J_m\left(\Theta^{(2)}_{m_F}\right) J_{n'}(\Theta^{(1)*}_{m_F}) J_{m'}\left(\Theta^{(2)*}_{m_F}\right) e^{i(n+m-n'-m')qz} \\ & \times e^{-iqv_0[(n-n')(T_2-T_1) + (n+m-n'-m')(t-T_2)]} e^{-i\omega_q\{(n^2-n'^2)(T_2-T_1) + [(n+m)^2 - (n'+m')^2](t-T_2)\}} \\ & \times e^{-iq(m_F\mathcal{F})[(n-n')(T_2^2 - T_1^2) + (n+m-n'-m')(t^2 - T_2^2)]/2M}. \end{aligned} \tag{A18}$$

Since the density distribution contains frequency components that depend only on the *difference* between interfering momentum states, we recast the sums over n' and m' in terms of $\nu\bar{N} = n - n'$ and $\nu = n' + m' - n - m$ (the integer difference between

momentum states after the first and second pulses, respectively):

$$\rho^{(2)}_{m_F m_F}(z,t) = -\frac{|\alpha_{m_F}|^2}{2\pi\hbar}\sum_{\nu,\bar{N},n,m} i^{\nu} J_n\left(\Theta^{(1)}_{m_F}\right) J_{n-\nu\bar{N}}\left(\Theta^{(1)*}_{m_F}\right) J_m\left(\Theta^{(2)}_{m_F}\right) J_{m+\nu(\bar{N}+1)}\left(\Theta^{(2)*}_{m_F}\right) e^{-i\nu q z} \times e^{i\nu q v_0[(t-T_2)-\bar{N}(T_2-T_1)]} e^{i\nu\omega_q\{[2(n+m)+\nu](t-T_2)-\bar{N}(2n-\nu\bar{N})(T_2-T_1)\}} e^{i\nu q(m_F\mathcal{F})[(t^2-T_2^2)-\bar{N}(T_2^2-T_1^2)]/2M}. \tag{A19}$$

The scattered field is proportional to the q-Fourier harmonic of $\rho^{(2)}_{m_F m_F}(z,t)$ [the coefficient of the $e^{-i\nu q z}$ term in Eq. (A19), with $\nu = 1$]. Summing over all magnetic sublevels in the ground state, one can show that

$$E^{(2)}_{\mathcal{F}}(t;\boldsymbol{T}) = \sum_{m_F} E^{(2)}_{m_F}(t;\boldsymbol{T}) e^{i m_F \phi^{(2)}_{\mathcal{F}}(t;\boldsymbol{T})}, \tag{A20}$$

where

$$E^{(2)}_{m_F}(t;\boldsymbol{T}) \propto |\alpha_{m_F}|^2 \left(C^{F\ 1\ F+1}_{m_F\ q_L\ m_F+q_L}\right)^2 \sum_{\bar{N}} (-1)^{\bar{N}+1} e^{-[(t-t^{(2)}_{\rm echo})/\tau_{\rm coh}]^2} e^{i q v_0 (t-t^{(2)}_{\rm echo})} \times J_{\bar{N}}\left(2u^{(1)}_{m_F}\sqrt{\sin(\varphi_1-\theta)\sin(\varphi_1+\theta)}\right) J_{\bar{N}+1}\left(2u^{(2)}_{m_F}\sqrt{\sin(\varphi_2-\theta)\sin(\varphi_2+\theta)}\right) \times \left(\frac{\sin(\varphi_1+\theta)}{\sin(\varphi_1-\theta)}\right)^{\bar{N}/2} \left(\frac{\sin(\varphi_2-\theta)}{\sin(\varphi_2+\theta)}\right)^{(\bar{N}+1)/2} \tag{A21}$$

is the field scattered from each magnetic sublevel, with recoil phases,

$$\varphi_1(t;\boldsymbol{T}) = \omega_q\left(t - t^{(2)}_{\rm echo}\right), \tag{A22a}$$

$$\varphi_2(t;\boldsymbol{T}) = \omega_q(t - T_2), \tag{A22b}$$

and $m_F\phi^{(2)}_{\mathcal{F}}$ is the phase shift of the density grating produced in the ground state $|F\, m_F\rangle$ due to the presence of the external force $\mathcal{F}$, with $\phi^{(2)}_{\mathcal{F}}$ given by

$$\phi^{(2)}_{\mathcal{F}}(t;\boldsymbol{T}) = \frac{q\mathcal{F}}{2M}\left[\left(t^2 - T_2^2\right) - \bar{N}\left(T_2^2 - T_1^2\right)\right]. \tag{A23}$$

In deriving Eq. (A21) we have made use of the Bessel function summation theorem [15,16,40],

$$\sum_n J_n(ue^{i\theta}) J_{n+\eta}(ue^{-i\theta}) e^{i(2n+\eta)\phi} = i^{\eta} J_{\eta}(2u\sqrt{\sin(\phi-\theta)\sin(\phi+\theta)}) \left(\frac{\sin(\phi-\theta)}{\sin(\phi+\theta)}\right)^{\eta/2}, \tag{A24}$$

and we averaged over the velocity distribution of the sample assuming a Maxwellian distribution centered at v_0 with e^{-1} width $\sigma_v = \sqrt{2k_B\mathcal{T}/M}$. In this way, we account for the possibility of an initial launch of the atomic cloud and for the dephasing of the echo due to the distribution of Doppler phases in the sample. An additional factor of $(C^{F\ 1\ F+1}_{m_F\ q_L\ m_F+q_L})^2$ was added to the scattered field to account for the atom-field coupling by the read-out pulse. The scattered field lasts for a time $\tau_{\rm coh} = 2/q\sigma_v$—called the coherence time—about each echo, which occur at times $t^{(2)}_{\rm echo} = \bar{N}(T_2 - T_1) + T_2$. The phase θ in Eq. (A21), associated with spontaneous emission during the excitation pulses, affects only the recoil-dependent component of the signal [16].

These results can be generalized for the case of an N-pulse interferometer with a set of onset times $\boldsymbol{T} = \{T_1, T_2, \ldots, T_N\}$ for which $T_{j+1} > T_j$. After N sw pulses, each with pulse area $u^{(j)}_{m_F}$, the total scattered field at time t is

$$E^{(N)}_{\mathcal{F}}(t;\boldsymbol{T}) = \sum_{m_F} E^{(N)}_{m_F}(t;\boldsymbol{T}) e^{i m_F \phi^{(N)}_{\mathcal{F}}(t;\boldsymbol{T})}, \tag{A25}$$

where

$$E^{(N)}_{m_F}(t;\boldsymbol{T}) \propto -|\alpha_{m_F}|^2 \left(C^{F\ 1\ F+1}_{m_F\ q_L\ m_F+q_L}\right)^2 \sum_{l_1,l_2,\ldots,l_{N-1}} e^{-[(t-t^{(N)}_{\rm echo})/\tau_{\rm coh}]^2} e^{i q v_0 (t-t^{(N)}_{\rm echo})} \times \prod_{j=1}^{N} J_{(l_j-l_{j-1})}\left(2u^{(j)}_{m_F}\sqrt{\sin(\varphi_j-\theta)\sin(\varphi_j+\theta)}\right) \left(\frac{\sin(\varphi_j-\theta)}{\sin(\varphi_j+\theta)}\right)^{(l_j-l_{j-1})/2}. \tag{A26}$$

Here, $\boldsymbol{l} = \{l_1, l_2, \ldots, l_N\}$ denotes the set of momentum states that interfere after the pulse sequence, where l_j is the difference between interfering momentum states (in units of $\hbar q$) after pulse j. The echo times and the recoil phases are

given by

$$t_{\text{echo}}^{(N)}(\boldsymbol{T}) = T_N - \frac{1}{l_N}\sum_{j=1}^{N-1} l_j(T_{j+1} - T_j), \tag{A27a}$$

$$\varphi_j(t;\boldsymbol{T}) = \omega_q \sum_{k=j}^{N} l_k(T_{k+1} - T_k), \tag{A27b}$$

and the contribution to the phase of the grating due to the force $\mathcal{F}$ is

$$\phi_{\mathcal{F}}^{(N)}(t;\boldsymbol{T}) = \frac{q\mathcal{F}}{2M}\sum_{j=1}^{N} l_j\left(T_{j+1}^2 - T_j^2\right). \tag{A28}$$

In Eqs. (A26)–(A28) $l_N = 1$, which corresponds to the scattered field from the q-Fourier harmonic of the density formed after the sw pulses, and it is understood that $l_0 = 0$ and $T_{N+1} = t$.

We now use the formalism for the N-pulse echo signal [Eq. (A26)] to obtain an expression for the three-pulse interferometer signal discussed in Sec. II. We begin by setting $N = 3$ and $\boldsymbol{T} = \{T_1, T_1 + T_{21}, T_1 + T_{21} + T_{32}\}$. For an echo to occur at $t_{\text{echo}}^{(3)} = T_1 + T_{32} + (\bar{N} + 1)T_{21}$ for any T_1, T_{32} and T_{21}, Eq. (A27a) dictates the set of l_j to be $\boldsymbol{l} = \{-\bar{N}, 0, 1\}$. Then, it can be shown that the scattered field is given by

$$\begin{aligned} E_{m_F}^{(3)}(t;\boldsymbol{T}) \propto |\alpha_{m_F}|^2 \left(C_{m_F\ q_L\ m_F+q_L}^{F\ 1\ F+1}\right)^2 \sum_{\bar{N}} (-1)^{\bar{N}+1} e^{-\left[\left(t - t_{\text{echo}}^{(3)}\right)/\tau_{\text{coh}}\right]^2} e^{iqv_0\left(t - t_{\text{echo}}^{(3)}\right)} \\ \times J_{\bar{N}}\left(2u_{m_F}^{(1)}\sqrt{\sin(\varphi_1 - \theta)\sin(\varphi_1 + \theta)}\right) J_{\bar{N}}\left(2u_{m_F}^{(2)}\sqrt{\sin(\varphi_2 - \theta)\sin(\varphi_2 + \theta)}\right) \\ \times J_1\left(2u_{m_F}^{(3)}\sqrt{\sin(\varphi_3 - \theta)\sin(\varphi_3 + \theta)}\right)\left(\frac{\sin(\varphi_1 + \theta)}{\sin(\varphi_1 - \theta)}\right)^{\bar{N}/2} \left(\frac{\sin(\varphi_2 - \theta)}{\sin(\varphi_2 + \theta)}\right)^{\bar{N}/2} \left(\frac{\sin(\varphi_3 - \theta)}{\sin(\varphi_3 + \theta)}\right)^{1/2}, \end{aligned} \tag{A29}$$

where the recoil phases in this case are

$$\varphi_1 = \omega_q\left(t - t_{\text{echo}}^{(3)}\right), \tag{A30a}$$

$$\varphi_2 = \varphi_3 = \omega_q\left(t - t_{\text{echo}}^{(3)} + \bar{N}T_{21}\right), \tag{A30b}$$

and the grating phase due to $\mathcal{F}$ is

$$\begin{aligned} \phi_{\mathcal{F}}^{(3)}(t;\boldsymbol{T}) &= \frac{q\mathcal{F}}{2M}\left[-\bar{N}\left(T_2^2 - T_1^2\right) + \left(t^2 - T_3^2\right)\right] \\ &= \frac{q\mathcal{F}}{2M}\left\{\bar{N}(\bar{N}+1)T_{21}^2 + 2\bar{N}T_{32}T_{21} + 2[T_1 + T_{32} + (\bar{N}+1)T_{21}]\Delta t + \Delta t^2\right\}. \end{aligned} \tag{A31}$$

[1] M. Kasevich and S. Chu, Phys. Rev. Lett. **67**, 181 (1991).
[2] A. Peters, K. Y. Chung, and S. Chu, Nature (London) **400**, 849 (1999).
[3] A. Peters, K. Y. Chung, and S. Chu, Metrologia **38**, 25 (2001).
[4] K. J. Hughes, J. H. T. Burke, and C. A. Sackett, Phys. Rev. Lett. **102**, 150403 (2009).
[5] N. Poli, F.-Y. Wang, M. G. Tarallo, A. Alberti, M. Prevedelli, and G. M. Tino, Phys. Rev. Lett. **106**, 038501 (2011).
[6] M. J. Snadden, J. M. McGuirk, P. Bouyer, K. G. Haritos, and M. A. Kasevich, Phys. Rev. Lett. **81**, 971 (1998).
[7] J. M. McGuirk, G. T. Foster, J. B. Fixler, M. J. Snadden, and M. A. Kasevich, Phys. Rev. A **65**, 033608 (2002).
[8] N. Yu, J. M. Kohel, J. R. Kellogg, and L. Maleki, Appl. Phys. B **84**, 647 (2006).
[9] T. L. Gustavson, P. Bouyer, and M. A. Kasevich, Phys. Rev. Lett. **78**, 2046 (1997).
[10] S. Wu, E. Su, and M. Prentiss, Phys. Rev. Lett. **99**, 173201 (2007).
[11] J. H. T. Burke and C. A. Sackett, Phys. Rev. A **80**, 061603 (2009).
[12] S. B. Cahn, A. Kumarakrishnan, U. Shim, T. Sleator, P. R. Berman, and B. Dubetsky, Phys. Rev. Lett. **79**, 784 (1997).
[13] D. V. Strekalov, A. Turlapov, A. Kumarakrishnan, and T. Sleator, Phys. Rev. A **66**, 023601 (2002).
[14] E. J. Su, S. Wu, and M. G. Prentiss, Phys. Rev. A **81**, 043631 (2010).
[15] S. Beattie, B. Barrett, M. Weel, I. Chan, C. Mok, S. B. Cahn, and A. Kumarakrishnan, Phys. Rev. A **77**, 013610 (2008).
[16] B. Barrett, I. Yavin, S. Beattie, and A. Kumarakrishnan, Phys. Rev. A **82**, 023625 (2010).
[17] T. W. Mossberg, R. Kachru, S. R. Hartmann, and A. M. Flusberg, Phys. Rev. A **20**, 1976 (1979).

[18] C. J. Bordé, C. Salomon, S. Avrillier, A. Van Lerberghe, C. Bréant, D. Bassi, and G. Scoles, Phys. Rev. A **30**, 1836 (1984).
[19] L. Allen and J. H. Eberly, *Optical Resonance and Two-Level Atoms* (Dover, New York, 1987).
[20] B. Dubetsky, P. R. Berman, and T. Sleator, Phys. Rev. A **46**, R2213 (1992).
[21] B. Barrett, I. Chan, C. Mok, A. Carew, I. Yavin, A. Kumarakrishnan, S. B. Cahn, and T. Sleator, in *Advances in Atomic, Molecular and Optical Physics*, Vol. 60, edited by E. Arimondo, P. R. Berman, and C. C. Lin (Elsevier, Amsterdam, 2011), Chap. 3.
[22] M. Weel and A. Kumarakrishnan, Phys. Rev. A **67**, 061602(R) (2003).
[23] S. Beattie, B. Barrett, I. Chan, C. Mok, I. Yavin, and A. Kumarakrishnan, Phys. Rev. A **79**, 021605(R) (2009).
[24] S. Beattie, B. Barrett, I. Chan, C. Mok, I. Yavin, and A. Kumarakrishnan, Phys. Rev. A **80**, 013618 (2009).
[25] B. Barrett, S. Beattie, A. Carew, I. Chan, C. Mok, I. Yavin, and A. Kumarakrishnan, in *Proceedings of ICONO 2010: International Conference on Coherent and Nonlinear Optics*, Vol. 7993, edited by C. Fabre, V. Zadkov, and K. Drabovich (SPIE, Bellingham, 2011), pp. 79930Y–1.
[26] M. Weel, I. Chan, S. Beattie, A. Kumarakrishnan, D. Gosset, and I. Yavin, Phys. Rev. A **73**, 063624 (2006).
[27] M. F. Andersen and T. Sleator, Phys. Rev. Lett. **103**, 070402 (2009).
[28] A. Wicht, J. M. Hensley, E. Sarajlic, and S. Chu, Phys. Scr. **T102**, 82 (2002).
[29] I. Chan, B. Barrett, and A. Kumarakrishnan, Phys. Rev. A **84**, 032509 (2011).
[30] T. M. Roach, J. Phys. B **37**, 3551 (2004).
[31] M.-K. Zhou, Z.-K. Hu, X.-C. Duan, B.-L. Sun, J.-B. Zhao, and J. Luo, Phys. Rev. A **82**, 061602(R) (2010).
[32] D. S. Weiss, E. Riss, Y. Shevy, P. J. Ungar, and S. Chu, J. Opt. Soc. Am. B **6**, 2072 (1989).
[33] A. Vorozcovs, M. Weel, S. Beattie, S. Cauchi, and A. Kumarakrishnan, J. Opt. Soc. Am. B **22**, 943 (2005).
[34] S. Slama, C. von Cube, M. Kohler, C. Zimmermann, and P. W. Courteille, Phys. Rev. A **73**, 023424 (2006).
[35] A. Schilke, C. Zimmermann, P. W. Courteille, and W. Guerin, Phys. Rev. Lett. **106**, 223903 (2011).
[36] T. M. Niebauer, G. S. Sasagawa, J. E. Faller, R. Hilt, and F. Klopping, Metrologia **32**, 159 (1995).
[37] J. Le Gouët, T. E. Mehlstäubler, J. Kim, S. Merlet, A. Clairon, A. Landragin, and F. P. D. Santos, Appl. Phys. B **92**, 133 (2008).
[38] B. Young, D. S. Bonomi, T. Patterson, F. Roller, T. Tran, A. Vitouchkine, T. Gustavson, and M. Kasevich, in *Proceedings of the International Conference on Laser Science* (Optical Society of America, Washington, DC., 2007), p. LTuH1.
[39] M. Suzuki, Commun. Math. Phys. **57**, 193 (1977).
[40] I. S. Gradshteyn and I. M. Ryzhik, *Tables of Integrals, Series, and Products*, 7th ed. (Elsevier, Amsterdam, 2007), p. 940.